Measurement Science
and Technology

100 year anniversary
Measurement Science and Technology

PURPOSE-LED
PUBLISHING™

PAPER • **OPEN ACCESS**

Offline circular path error measurement and compensation for robotic machining applications

To cite this article: Kanglin Xing *et al* 2025 *Meas. Sci. Technol.* **36** 106005

View the article online for updates and enhancements.

You may also like

- Photonic-digital hybrid artificial intelligence hardware architectures: at the interface of the real and virtual worlds
Lília M S Dias, Dinis O Abranches, Ana R Bastos et al.

- ICRH modelling of DTT in full power and reduced-field plasma scenarios using full wave codes
A Cardinali, C Castaldo, F Napoli et al.

- Low-noise anisotropic magnetoresistance sensing at human body temperature: unveiling the optimal doping in $La_{1-x}Sr_xMnO_3$ films
Raul Solis Leon, Ines Garcia Manuz, Sandeep Kumar Chaluvadi et al.

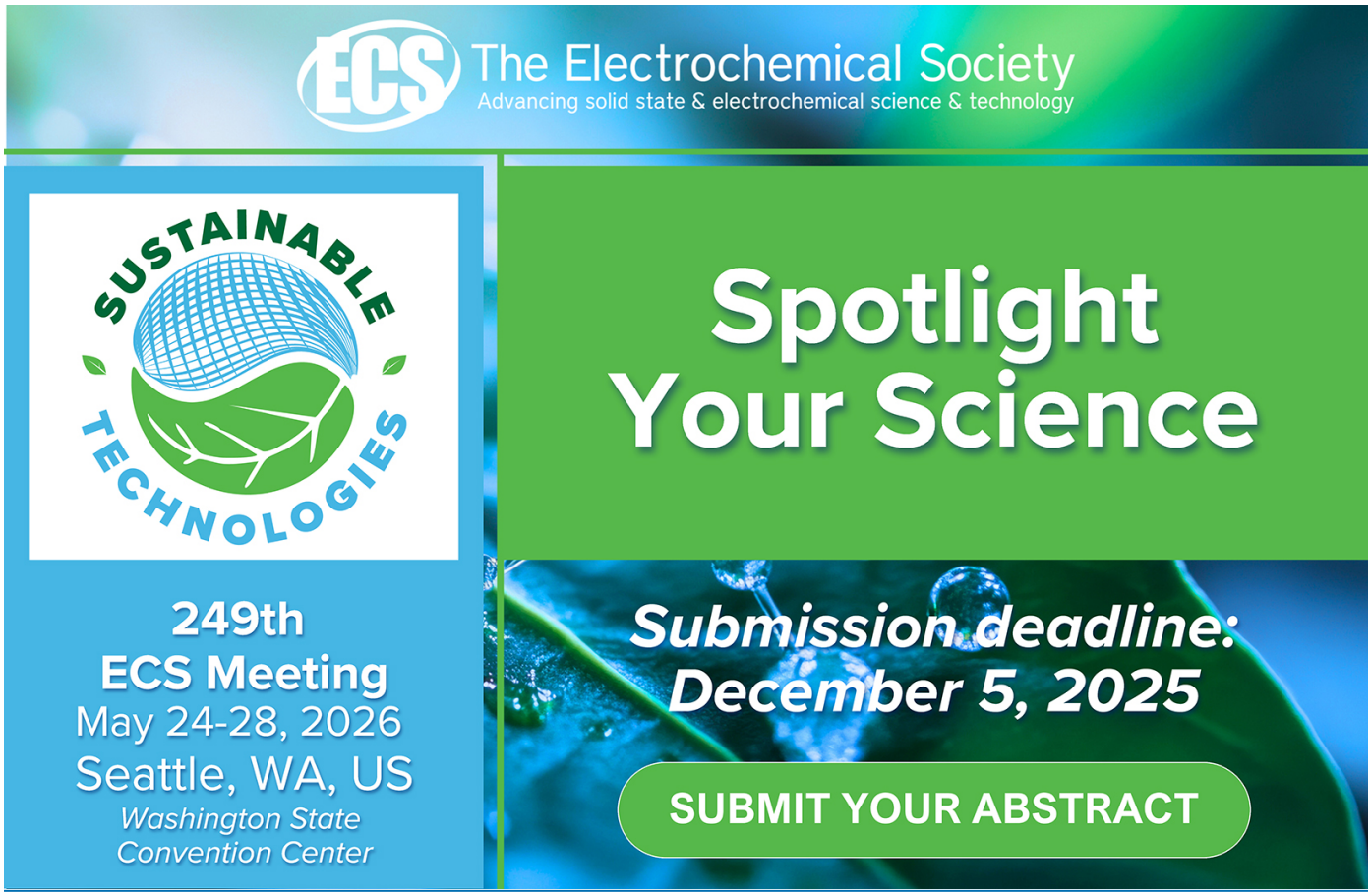

This content was downloaded from IP address 142.137.251.24 on 14/11/2025 at 20:26

OPEN ACCESS
IOP Publishing
Measurement Science and Technology
Meas. Sci. Technol. **36** (2025) 106005 (24pp)
https://doi.org/10.1088/1361-6501/ae0e3d

Offline circular path error measurement and compensation for robotic machining applications

Kanglin Xing[1], Yannick Cianyi[1], Ilian A Bonev[2], Henri Champliaud[1] and Zhaoheng Liu[1,*]

[1] Department of Mechanical Engineering, École de technologie supérieure, 1100, Notre-Dame St W, Montreal, Quebec H3C 1K3, Canada
[2] Department of Systems Engineering, École de technologie supérieure, 1100, Notre-Dame St W, Montreal, Quebec H3C 1K3, Canada

E-mail: zhaoheng.liu@etsmtl.ca

Received 17 June 2025, revised 16 September 2025
Accepted for publication 1 October 2025
Published 14 October 2025

Abstract

Robotic machining provides a flexible and cost-effective alternative to conventional machine tools. However, robots have relatively poor rigidity and accuracy. Performance enhancement in robotic machining typically relies on machining parameter optimization, robot calibration, offline or online path error compensation, and process refinement. This study focuses on offline measurement and compensation of circular path errors using a telescoping ballbar system. To address the inherent limitations of traditional ballbar setups, particularly their restriction to a few fixed measurement radii, a novel out-of-plane ballbar measurement method is introduced along with a custom data processing framework. This configuration enabled error measurements across general circular trajectories with varying radii. A geometric projection model was developed to quantify the measurement distortion induced by the out-of-plane angle and a small-radius adaptor was designed to extend the applicability of the ballbar system. The proposed method was experimentally validated on a robotic machining platform using a laser tracker. The results show that at out-of-plane angles below 30°, the system achieves over 61% compensation accuracy, which is comparable to the 75% achieved using the laser tracker, while requiring less than 20% hardware cost. These findings demonstrate that the proposed approach offers a practical, scalable, and economical solution for circular-path error compensation in robotic machining.

Keywords: circular path error, error compensation, hexapod machining cell, telescoping ballbar, laser tracker

* Author to whom any correspondence should be addressed.

Original content from this work may be used under the terms of the Creative Commons Attribution 4.0 licence. Any further distribution of this work must maintain attribution to the author(s) and the title of the work, journal citation and DOI.

© 2025 The Author(s). Published by IOP Publishing Ltd

Nomenclature

AF	Amplification factor
SMR	Spherically mounted retroreflector
TCP	Tool center position
PAM	Procrustes analysis method
ADM	Absolute distance meter
P2P	Point-to-point method
CD	Circular deviation
CCW	Counter-clockwise
CW	Clockwise
DPM	Dynamic path modification

1. Introduction

Industrial robots have become increasingly attractive for manufacturing applications owing to their flexibility and cost efficiency. However, their relatively poor accuracy significantly affects the performance of certain manufacturing applications [1]. Positioning errors primarily arise from geometric factors, such as machining accuracy, assembly deviations, and wear, as well as from non-geometric factors, including ambient temperature fluctuations, control system stability, and vibration [2]. To address this problem, path error compensation techniques are essential.

General path-error compensation strategies for industrial robots are classified into two categories: offline and online compensation methods [3]. Offline error compensation primarily involves calibrating the robot's parameters using tools such as laser trackers, coordinate measuring machines [4–7] and touch trigger probes [8]. While effective at correcting static structural errors, offline strategies are inherently limited by their inability to capture dynamic path deviations caused by operational loads, vibrations, or temperature fluctuations [9]. In contrast, online strategies account for dynamic path errors, thereby addressing the limitations of offline methods. Consequently, online compensation is typically implemented in conjunction with an offline calibration. Based on measurement data sources and compensation principles, online error compensation strategies can be categorized into semi-closed-loop compensation, which relies on joint feedback, and fully closed-loop compensation, which utilizes endpoint feedback. Typical tools for online closed-loop path error compensation include grating rulers [10], laser trackers [3, 11] and photogrammetry devices [1, 12–16]. By applying real-time pose-correction algorithms, these systems have demonstrated sub-100 μm accuracy levels on various industrial robot platforms. For instance, a Fanuc M20-iA robot achieved an absolute positioning accuracy of ±50 μm [12], whereas a KUKA KR6 R700 robot reduced single-point errors to 58 μm [3]. However, such systems are often expensive and difficult to deploy in shop-floor environments or in flexible robotic machining cells. In addition, the accuracy of laser trackers and photogrammetry devices is inherently limited by their measurement range and setup conditions. For example, the FARO laser tracker typically offers an accuracy of approximately 30 μm, whereas C-Track 780 provides a volumetric accuracy of approximately 65 μm. In contrast, the ballbar system has a resolution of 0.1 μm and measurement accuracy of approximately ± (0.7 + 0.3%L) μm (e.g. Renishaw QC20-W, where L denotes the measured displacement in millimeters between the two ballbar pivot points during motion, typically corresponding to the radius of the circular trajectory under test) and is easy to use, portable, and affordable. These characteristics make it an attractive alternative for on-site circular path verification, particularly in specific environments where deploying high-end tracking systems is impractical.

Previous studies have demonstrated the feasibility of employing a telescoping ballbar for robot calibration and accuracy evaluation. A novel 6D measurement system using a single telescoping ballbar with magnetic cups was proposed for absolute calibration of a six-axis robot [17]. This approach achieved sub-millimeter positioning accuracy (0.479 mm) over 72 discrete poses without relying on high-end metrology tools. However, its effectiveness is limited to fixed magnetic configurations, which lack flexibility for arbitrary path shapes or angular tool installation. Another study [18] extended the ballbar methodology to a helical path configuration and employed the Taguchi method to optimize the measurement parameters, including the feed speed, ballbar radius, and pitch. This study emphasizes the sensitivity of error measurement to configuration variables and introduces a regression-based predictive model for estimating compensation outcomes under various machining conditions.

Although both studies confirmed the potential of ballbar systems for high-resolution error characterization, practical challenges, such as variable-radius paths, angular ballbar arrangements, and flexible fixture setups required in dynamic shop-floor environments, have not been addressed. Furthermore, commercial systems such as Renishaw RCS L-90 offer integrated solutions for industrial robot calibration by utilizing a fixture-mounted ballbar in conjunction with proprietary software routines. Although these systems support the automated setup of the TCP and part frames, they rely heavily on standardized test procedures and rigid mechanical structures. The central pillar and hollow ball fixture configurations were designed for fixed-radius linear or circular motion paths with limited adaptability to small-radius or non-planar trajectories. Furthermore, Renishaw RCS software operates in a closed environment, preventing user access to raw measurement data or algorithm customization. These factors restrict the application of RCS L-90 to static, high-throughput production settings, making it unsuitable for flexible or research-driven robotic machining scenarios in which path geometries and orientations vary dynamically.

Although ballbar systems provide high resolution and practical advantages, their application has traditionally been limited to a discrete set of circular path radii (e.g. 50 mm, 100 mm, 150 mm, and 300 mm), thereby limiting their flexibility in robotic applications. Furthermore, the effectiveness of circular path error compensation is determined not only by the resolution of the measurement system, but also by the sampling rate, selected compensation algorithm, and adaptability of the hardware to varying trajectory configurations.

Although these factors significantly influence performance, a unified framework that systematically incorporates them, particularly in the context of small- or variable-radius trajectories, has not yet been established. In addition, current ballbar systems lack methodological guidelines for generalized deployment in flexible robotic machining environments, particularly in cases involving out-of-plane mounting or noncircular path geometries.

To bridge this gap, a more adaptable and cost-effective strategy is required, one that can accommodate variable-radius circular trajectories, offer high measurement resolution, and support integration with flexible robotic setups.

In response to these challenges, this study proposes an out-of-plane ballbar circular path error measurement and compensation method that incorporates an out-of-plane angular installation setup to enable flexible alignment with different trajectory planes, a custom-designed small-radius adaptor to extend the effective range of the ballbar, and a geometric projection model that quantifies installation-angle-induced distortion and guides practical configuration. The proposed method was experimentally validated on a robotic hexapod platform and compared with a laser tracker. The results demonstrate that when installed at optimized angles (e.g. less than 30°), the ballbar system achieves a compensation rate exceeding 61%, comparable to the 75% achieved by the laser tracker, while operating at less than 20% of the hardware cost.

The remainder of this paper is structured as follows: the next section outlines the circular path error measurement and compensation methods; section 3 details the experimental platform and validation setups; sections 4 and 5 present the results and discussion, respectively; and section 6 concludes with a summary and directions for future work.

2. Circular path error measurement and compensation method

Industrial robots inherently exhibit space motion errors, which originate from geometric deviations, thermal effects, servo control limitations, and structural compliance under load [2, 7]. These errors manifest along different directions of the end-effector trajectory. In the case of circular motions, the most representative component is the radial error, defined as the deviation between the actual and nominal circular paths in the radial direction. In other words, the radial error can be regarded as the projection of the robot's space motion errors onto the radial direction of the circular trajectory [4, 9, 17]. This study therefore focuses on measuring and compensating such radial errors using an out-of-plane ballbar setup and a dedicated compensation framework.

2.1. Circular path measurement using ballbar at multiple radii

Circular path errors can be measured using online or offline tools such as a ballbar, laser tracker, laser ballbar, C-track, or VXtrack system. These tools differ in their measurement range, precision, sampling rate, and cost. Ballbars, including laser ballbar, offer a smaller measurement range, but higher precision. In contrast, laser trackers provide the largest measurement range with a precision of approximately 10–50 μm. In addition, the ballbar primarily operates in a 2D plane, whereas the laser tracker, laser ballbar, C-Track [13], and VXtrack systems measure the 3D positions of the measurement targets. Given the commonality of these measurement tools, the ballbar and laser tracker were selected as representative instruments for circular path error measurements in this study.

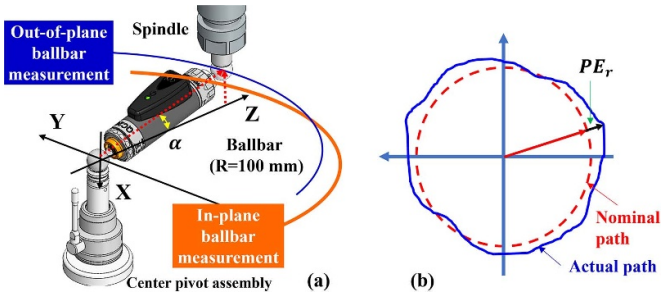

Figure 1. (a) Ballbar setup for circular path error measurement-in-plane and out-of-plane measurement methods; (b) path error measured by ballbar.

The general ballbar test was conducted within the 2D plane of the machine's coordinate system (in-plane measurement), following a circular path at a specified feeding speed and given testing radius (e.g. 50, 100, 150, and 300), as shown in figure 1(a). In this setup, the ballbar serves as a linear displacement sensor to measure the path error (PE_r), which is defined by the difference between the actual circular path and nominal circular path, as shown in figure 1(b) and equation (1). Commercial ballbar software is specifically designed for machine tool error measurements and cannot be directly applied to circular path error measurements. However, raw data can be accurately captured at a constant sampling rate of 1000 Hz by utilizing an application programming interface (API) provided with ballbar software [19, 20]. Under this sampling rate, a sufficient circular path error can be acquired for compensation. In this study, the term 'out-of-plane ballbar measurement' refers to the configuration in which the robot follows a circular trajectory with a radius smaller than the length of the ballbar, resulting in the ballbar sweeping a conical surface rather than remaining confined to a single measurement plane.

Commercial ballbar systems are limited to measurements performed at several fixed radii. However, holes or tubes of varying dimensions are often encountered or required in practical applications. To broaden its application range, a novel ballbar measurement method and data processing approach are proposed in this study (figure 2). By installing the ballbar at a specific out-of-plane angle with respect to the plane of the circular path, it was possible to measure the radial path errors (PE_{ra}) at smaller radii, as illustrated in figure 2. In this study, this configuration is abbreviated as an out-of-plane

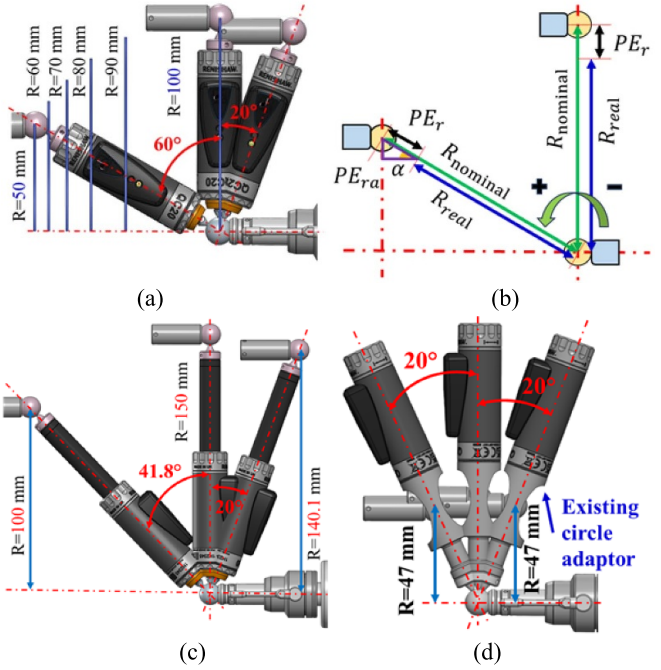

Figure 2. (a) Ballbar installation for other radius error measurement (example, R = 100 mm); (b) path error measured by a ballbar with a radius of 100 mm at a specific out-of-plane angle; (c) installation and measurement range for a ballbar with a radius of 150 mm; (d) installation and measurement range of a ballbar with a radius of 50 mm.

ballbar measurement. The proposed measurement can be configured with an out-of-plane angle α in either negative or positive direction. A positive inclination helps avoid most interferences between the ballbar and the pivot assembly. In contrast, a negative inclination may cause interference, particularly when using a ballbar in the 50 mm setup, as shown in figure 2(d). However, a positive inclination allows the spindle to be much closer to the actual cutting plane because the pivot assembly has a considerable height that already offsets the measurement plane too much.

By applying this principle, the measurement span of the ballbar could be widened to encompass a larger range of radii. For instance, a ballbar with a nominal radius of 100 mm can be adapted to measure smaller radii of down to 50 mm when using positive inclination, or down to approximately 87 mm when using negative inclination, as shown in figure 2(a). Similarly, a ballbar with a nominal radius of 150 mm can measure smaller radii of down to 100 mm using positive inclination or down to approximately 140 mm when using negative inclination, as shown in figure 2(c).

In the case of Renishaw's ballbar with a small-circle adaptor for measuring with a radius of 50 mm, the measurement radius can only be decreased to approximately 47 mm with both positive and negative inclinations, as shown in figure 2(d). To allow for the measurement of smaller radii, an improved small-circle adaptor was designed and machined, as shown in figure 3(a). With this new adaptor, circular paths

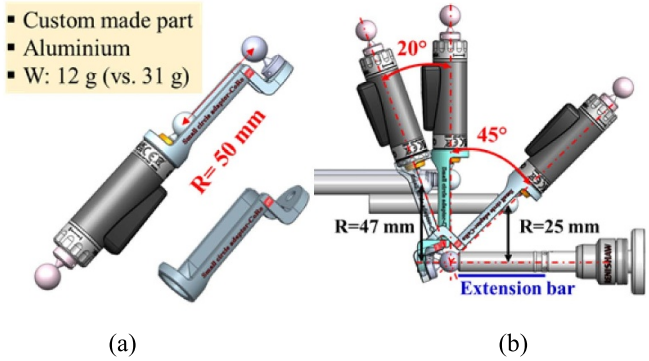

Figure 3. (a) The new, improved small-circle adaptor; (b) installation and measurement range of ballbar with the new small-circle adaptor.

with radii as small as 25 mm can be measured, as shown in figure 3(b). The adaptor was machined from aluminum 6061 and subsequently anodized to increase surface hardness, wear resistance, and corrosion resistance. The design adopts a one-piece structure, and the ball cup is fixed by screws to ensure stable attachment during repeated installations and robot motions.

Unlike the standard ballbar setup, which operates within a single measurement plane and provides results that are directly applicable to path-error compensation (equations (1) and (2)), R_{Real} stands for the true measured radial error and R_{Nominal} stands for the nominal radial error). The out-of-plane ballbar measurement requires additional calculations to determine the radial error at a specific radius. The hypothesis is that there is no or negligible minor axial movement along the vertical direction within the plane of the circular path. Assuming that the out-of-plane angle between the ballbar and the plane of the path is α, the circular path error PE_{ra} and the compensation value for each circular path COMPE_{ra} can be calculated using equations (3) and (4). When $\alpha = 0°$, the ballbar functions as in the standard ballbar measurement, resulting in $\text{PE}_{ra} = \text{PE}_r$,

$$\text{PE}_r = R_{\text{Real}} - R_{\text{Nominal}} \tag{1}$$

$$\text{COMPE}_r = -\text{PE}_r \tag{2}$$

$$\text{PE}_{ra} = \cos\alpha * (R_{\text{Real}} - R_{\text{Nominal}}) \tag{3}$$

$$\text{COMPE}_{ra} = -\text{PE}_{ra}. \tag{4}$$

2.2. Theoretical analysis of out-of-plane ballbar measurement and error projection

The process of measuring radial errors using a ballbar measured at an out-of-plane angle can be understood as a geometric projection of the true radial error vector onto the measurement axis of the ballbar. This setup inherently introduces

projection-induced measurement distortion, particularly as the out-of-plane angle increases.

Let the true radial error vector lie in the *YZ* circular path plane and let the ballbar be inclined at an out-of-plane angle α relative to that plane. The ballbar only measures the component of the true error along its own axis, resulting in the projection relationship shown in equation (3), to describe the distortion effect quantitatively, a parameter of the AF is defined as

$$\mathrm{AF} = 1/\cos(\alpha). \tag{5}$$

The AF shows the extent to which the actual error was underestimated during the measurement process. As the angle increases: when $\alpha = 10$–$20°$, AF ≈ 1.0, indicating minimal distortion; when $\alpha = 30°$, AF ≈ 1.155, corresponding to $\sim$15.5% amplification; when $\alpha = 45°$, AF ≈ 1.414, indicating over 40% amplification; $\alpha > 30°$, the distortion grows rapidly, with AF being more than 2. Such distortion can significantly degrade the accuracy and reliability of radial error measurements, especially in high-precision robotic machining tasks.

In addition to radial error projection distortion, the proposed method introduces another form of error propagation, namely, axial disturbances (along the *X*-axis, defined by our testing platform) that can corrupt the radial measurement. When PE_r is the true radial error, ΔX is an unintended axial disturbance. Subsequently, the composite-measured error becomes

$$\mathrm{CME}_{ra} = \sqrt{(\mathrm{PE}_r * \cos(\alpha))^2 + (\Delta X * \sin(\alpha))^2}. \tag{6}$$

This equation reveals a two-fold interaction: the true radial component is attenuated by the projection factor, whereas the axial disturbance is amplified by $\sin(\alpha)$ and superimposed onto the radial projection, thereby distorting the measured result. From this relationship, it can be inferred that at small installation angles (e.g. $\alpha < 10°$), the influence of ΔX is negligible. Under such conditions, the measurement predominantly reflects the true radial error, resulting in a high accuracy and low noise. In contrast, at moderate to large angles (e.g. $\alpha > 45°$), the value of $\sin(\alpha)$ increases substantially, allowing even minor axial disturbances to be projected onto the measurement axis. This leads to amplified noise and a decreased reliability of the radial error signal. At extreme angles (e.g.$\alpha = 90°$), the contribution from the radial projection becomes minimal, whereas the axial projection becomes dominant. Consequently, the measured signal is almost entirely governed by the cross-axis noise.

Building on the above projection analysis and the AF, we derive a first-order linearized model that makes the angle-dependent error terms explicit. Let the nominal circular path lie on the *YZ*-plane with unit vectors e_r, e_t, e_x (radial, tangential, and out-of-plane). When the ballbar is tilted by an out-of-plane angle α, its unit direction is $u_\alpha = \cos\alpha \cdot e_r + \sin\alpha \cdot e_x$. Denote the small in-plane radial deviation by PE_{ra}, the out-of-plane deviation by ΔX, and measurement/timing noise by ε. A first-order linearization around the nominal pose yields the measured ballbar increment, Δm, (equals to CME of equation (6))

$$\Delta m \approx \mathrm{PE}_{ra} \cdot \cos\alpha + \Delta x \cdot \sin\alpha + \varepsilon. \tag{7}$$

Following the geometric projection used in this work, the radial component is reconstructed by dividing by Cos α

$$\widehat{\mathrm{PE}_{ra}} = \frac{\Delta m}{\cos\alpha}. \tag{8}$$

The resulting reconstruction error along the radial direction (Δ_r) is therefore

$$\Delta_\mathrm{r} = \widehat{\mathrm{PE}_{ra}} - \mathrm{PE}_{ra} \approx \Delta x \cdot \tan\alpha + \frac{\varepsilon}{\cos\alpha}. \tag{9}$$

The equations (7)–(9) expose two angle-dependent channels behind the rapid distortion growth- $\Delta x \cdot \tan\alpha$ (cross-axis contamination) and $\varepsilon/\cos\alpha$ (projection amplification)-which explain the observed degradation at large angles (see section 4.2). A complete derivation is provided in appendix A1.

To ensure reliable and consistent measurement outcomes, it is recommended that the ballbar out-of-plane angle should be maintained below 30°. If larger angles are unavoidable, additional vibration isolation should be applied or compensation for axial disturbances should be implemented.

2.3. Circular path error compensation strategy

Circular path error compensation methods can be classified into two types: online and offline path error compensation methods. Their selection is related to circular path generation methods. Robot motion planning typically employs two types of motion control: P2P (figure 4(a)) and continuous-path methods [21, 22]. The P2P, which is the most commonly used method, guides the robot through specified points, thereby allowing it to infer the resulting trajectory. The control points were interconnected by multiple small linear segments. By contrast, continuous-path control estimates the end-effector's velocity and position at each point along the trajectory, enabling smoother motion. There are two command-circle arc motions and circular motions for FANUC robots (figures 4(b) and (c)). Circular arc motion commands offer more control for applications requiring precision and customization of arcs, whereas circular motion commands provide a simpler way to define circular trajectories based on geometric points (a minimum of three points). Motion planning can be selected based on several criteria: runtime, energy consumption, and smoothness of the motion path [23, 24]. The primary issue with P2P motion is the feed rate fluctuation at junction points, which can produce sharp trajectories and lead to unwanted vibrations [25]. This effect can be minimized by implementing trapezoidal or bell-shaped velocity profiles (using cubic, quartic, or quintic polynomials) [26] or by employing a novel control strategy that accounts for joint variables and velocity vectors [21].

Effective path error compensation requires the measured path errors to be accurately incorporated into the precise control points of a circular trajectory. Depending on the method

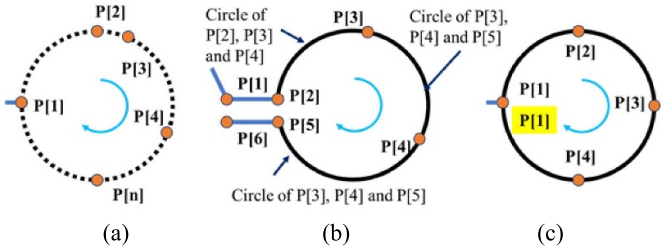

Figure 4. (a) Point-to-point strategy for circular path generation, the number of the used points is n; (b) circle arc motion command based continuous-path strategy for circular path generation, this example is with four controlling points; (c) circular motion command for generating of continuous circular path.

used for circular path generation, the approaches differ; for the circular motion method, only five control points are minimally required to generate the circular path. However, this limited number of control points does not allow comprehensive compensation to achieve a perfect circle. Thus, this method is suitable for online path-error compensation. In contrast, P2P and circular arc motion methods require a significantly larger number of control points to generate a highly accurate circular path. Consequently, these methods are better suited for offline path-error compensation, where precise adjustments can be applied to each control point. Once circular path errors are measured, they can be incorporated as compensation values into the target position for error correction. Compensation can be performed using either online or offline methods. In this study, only the offline circular-path error compensation method is implemented. The online path error compensation method, integrating the DPM function of the FANUC robot, will be proposed in future work.

For the measured radial error PE_i ($i = 1 \ldots N$), the offline path error generation method employs N_1 control points for the circular path generation in the YZ plane. Given that the sampling rates of the ballbar and laser tracker are 1000 Hz and 500 Hz, respectively, the size of the radial error dataset typically exceeds the number of control points (N1) that define the circular path. Consequently, the compensation value for each control point and the new coordinates of the controlling positions were calculated using the following equations (10)–(14).

Put it in detail, raw ballbar measurements were continuously recorded at 1000 Hz while the robot executed the commanded circular trajectory. Consistent with equations (10)–(14), the circle was partitioned into N1 equal angular intervals with step α. All high-rate ballbar samples were mapped to these angular intervals; for interval j, the mean radial deviation was computed from the samples falling in that sector. This angular resampling establishes a one-to-one association between each compensation value and a commanded control point, avoiding issues related to clock-level time drift between the measurement stream and the robot controller. Given that the 1000 Hz ballbar stream may contain outliers caused by sporadic vibration, communication jitter, or axial disturbances under out-of-plane conditions, taking a simple mean can bias the interval error and reduce the stability and reproducibility of the compensation. Therefore, before computing the interval average used in equation (9), we apply a simple within-interval three-sigma filter. For each angular interval, first compute the preliminary average and standard deviation from all ballbar samples falling in that interval. Discard any samples whose absolute deviation from the preliminary average exceeds three times the standard deviation. Recompute the average from the remaining samples and use this value as the interval error for equation (9).

Notably, the laser tracker can capture the 3D coordinates of each control position. For an equitable comparison with the ballbar, the same compensation strategy was applied, incorporating the compensation values along the Y- and Z-axes. The newly calculated positions were imputed into the FANUC program for the next measurement for the path error compensation tests:

$$A = \mathrm{round}\left(N/N_1\right) \tag{10}$$

$$\alpha = 360^\circ/N_1 \tag{11}$$

$$\mathrm{PE}_{C_j} = \mathrm{mean}\left(\mathrm{PE}_{C_{1+A(N_1-1)}} : \mathrm{PE}_{C_{A+A(N_1-1)}}\right) \quad j \in [1, N_1] \tag{12}$$

$$Z_j = \left(R + \mathrm{PE}_{C_j}\right)\cos\left(\alpha * j\right) \tag{13}$$

$$Y_j = \left(R + \mathrm{PE}_{C_j}\right)\sin\left(\alpha * j\right). \tag{14}$$

2.4. Key factors influencing compensation performance

The effectiveness of compensating for circular path errors depends on factors such as the error measurement method, path generation approach, radius of the circular path, and the sampling rate of the measurement devices. As discussed in the abstract, various tools can be employed for path error measurement, each differing in sampling rate, resolution, and ability to measure in a 2D plane or 3D space. In this study, a ballbar and laser tracker with sampling rates of 1000 Hz and 500 Hz, respectively, were utilized. For circular path generation in industrial robots, three methods were examined: P2P, circular motion, and circular arc motion. These methods require a varying number of control points, with circular motion requiring a minimum of five control points, whereas the other two methods demand more. Ideally, a smaller circular radius results in reduced path errors, thereby facilitating more effective path compensation.

In addition, the sampling rate, feed speed, controlling point number, and circular path radius can influence each other. Understanding these relationships is crucial for an effective offline path error compensation. When employing the offline circular path error compensation method, smaller line segments or arcs are preferred to generate a precise circular path.

Assuming that the number of control points for the circular path is N_2, the feed speed is F (mm min^{-1}), and the circular path radius is R (mm), the minimum required sampling rate f_s (Hz) can be expressed as:

$$f_s = \frac{N_2 F}{120\pi R}. \tag{15}$$

In the out-of-plane ballbar setup, variations in the ballbar radius influenced the possible out-of-plane angle. The measured radial error component of the ballbar also changed when projected onto the axial and radial error directions. These changes may impact the accuracy of the radial error measurements and potentially affect the circular path error compensation. These factors were examined through subsequent experimental results and theoretical analyzes.

3. Experimental platform and validation setup

3.1. Ballbar-based measurement implementation

Tests for circular path error compensation were conducted on a hexapod-machining cell comprising two Fanuc F200i hexapods (figure 5(a)). During these measurements, the hexapod mounted on the wall remained stationary, whereas that installed on the floor performed the required circular motion. Circular path error measurements were performed using a Renishaw Q20-W ballbar and a Faro ION laser tracker (figures 5(a) and (b)). The ballbar with a radius of 100 mm has a measurement range of ±1 mm, a resolution of 0.1 μm, and a sampling rate of 1000 Hz. Notably, an API-based, custom-developed program enabled the ballbar to achieve a maximum sampling rate of 1000 Hz. The actual sampling rate can be modified using the resampling operation. For the Faro laser tracker, operating in ADM mode, the resolution and accuracy were 0.5 μm and 8.8 μm, respectively, within a measurement range of 2 m. To synchronize data acquisition between the ballbar and laser tracker in one measurement process, a specialized fixture connecting two center cups was developed. The SMR of the laser tracker was mounted on the central cup, whereas the ballbar center ball was positioned on the end-side cup. The motor rotation lock was secured to the underside of the spindle to compensate for the absence of an anti-rotation component on the spindle (figures 5(c) and (d)). Before the measurement, a pre-heating operation of 1 h free movement of the hexapod floor was conducted. In addition, ballbar measurements were conducted in CCW and CW directions.

A series of experiments was conducted to investigate the relationship between various factors and circular path error compensation. To compare circular path error compensation methods, a ballbar with radii of 50 mm and 100 mm, as well as a laser tracker, were employed under a consistent robotic setup. Two repeated measurements were performed for each test.

The influence of factors, including sampling rate, feed speed, number of control points for the circular path, and circular path radius, on error compensation was examined. Based on the theoretical relationships among these factors, sampling

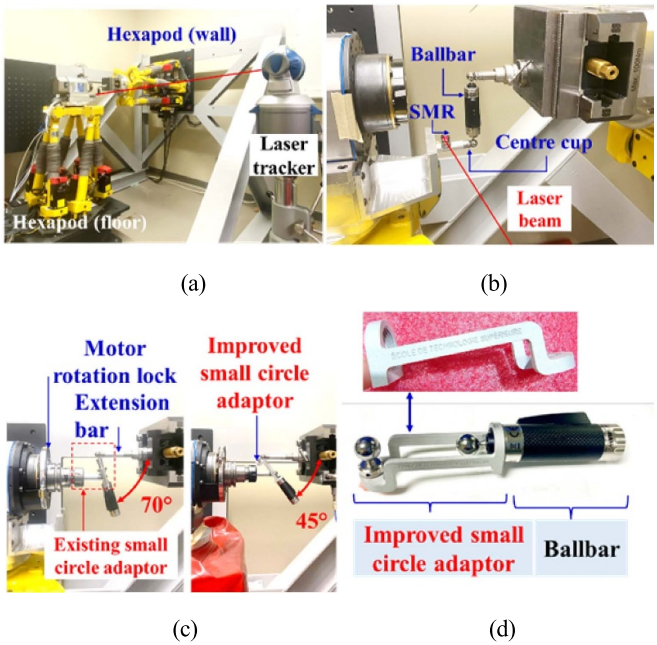

Figure 5. (a) Circular path error measurement using ballbar and laser tracker; (b) fixture for the synchronization of data acquisition of ballbar and laser tracker in one measurement process; (c) improved small circle adaptor; (d) installation of ballbar with the existing/improved small circle adaptor for circular path error measurement.

rates of 30, 50, 100, 250, 500, and 1000 Hz were used to assess their effects on the ballbar measurements. Furthermore, for a ballbar with a radius of 50 mm, tests were conducted at feed speeds of 1200, 1800, 2400, and 3000 mm min^{-1}, with sampling rates of 50, 100, and 1000 Hz. To explore the possibility of setting up a ballbar with varying radii (non-reference radius) for path error measurement and compensation, for a given ballbar with a radius of 100 mm, testing radii of 50, 60, 70, 80, and 90 were performed using the Arc-based circular path generation method.

3.2. Reference measurement using laser tracker

A laser tracker is a portable, large-scale measurement instrument that uses a laser beam to perform precise measurements of reflective targets installed in a 3D space [27]. It directs the laser beam toward a reflector, which consists of mirrors, and determines the distance and horizontal and vertical angles formed between the laser tracker and the reflector by analyzing the light pulses. The exact position of the reflector can be calculated using one distance and two angles. Herein, a laser tracker was used for coordinate alignment (figure 6).

The measurement of the circular path error, as well as the comparative analysis of the ballbar and laser tracker systems, requires the precise determination of the offset of the SMR relative to the TCP. TCP is defined as the tool cup used for a ballbar connection. Accurate measurement of this offset is critical because it significantly influences the overall accuracy of the robot. Potential methods for determining these parameters

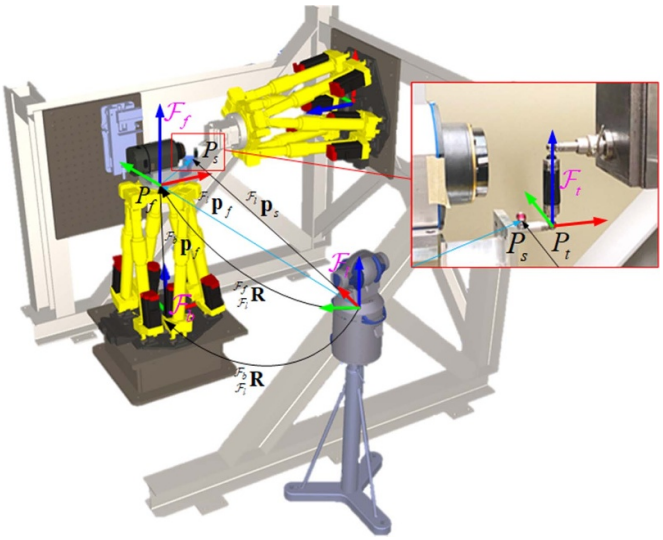

Figure 6. Setup of laser tracker for robot frame and laser tracker frame alignment.

include manual adjustment, offline calibration processes, automatic resolution as unknowns alongside the kinematic parameters of the robot, and performing three-axis rotations of all coordinate planes [9]. In this study, the proposed method [9] was employed (figure 7). The first step was to measure the positions of the SMR during the rotation of the hexapod platform about the *X*-, *Y*-, and *Z* axis. The measured SMR position data are shown in figure 8. We can work around to find the center C_i of the circle fitting data Γ_i, with $i = x, y, z$. using a three-dimensional least-squares fitting method, as described in figure 4(b). The location of the hexapod flange was then obtained using each of the following equations:

$$^{\mathcal{F}_l}\boldsymbol{P}_f = \begin{cases} ^{\mathcal{F}_l}\boldsymbol{P}_{C_z} + d_1\boldsymbol{n}_z; \text{ or} \\ ^{\mathcal{F}_l}\boldsymbol{P}_{C_x} + d_2\boldsymbol{n}_x; \text{ or} \\ ^{\mathcal{F}_l}\boldsymbol{P}_{C_y} + d_3\boldsymbol{n}_y \end{cases} \tag{16}$$

where $^{\mathcal{F}_l}\boldsymbol{P}_{C_i}$ is the position of the center of circle Γ_i with respect to the laser tracker frame $\mathcal{F}_l$, and.

$$d_1 = \|(C_yC_z)\cdot\boldsymbol{n}_z\| \tag{17}$$

$$d_2 = \|(C_yC_x)\cdot\boldsymbol{n}_x\| \tag{18}$$

$$d_3 = \|(C_xC_y)\cdot\boldsymbol{n}_y\|. \tag{19}$$

Are the *x, y*, and *z* components of the offset vector between the hexapod flange and SMR positions, as shown in figure 7(b). This offset can be expressed with respect to the laser tracker frame as

$$^{\mathcal{F}_l}\boldsymbol{P}_{sf} = \widetilde{^{\mathcal{F}_l}\boldsymbol{P}_s} - {}^{\mathcal{F}_l}\boldsymbol{P}_f = {}^{\mathcal{F}_l}\boldsymbol{r}_{P_fP_s}. \tag{20}$$

The symbol $\widetilde{\bullet}$ refers to the measured data.

Utilizing the calculated flange center coordinates, along with the positions of SMR and TCP, the rotation matrix from

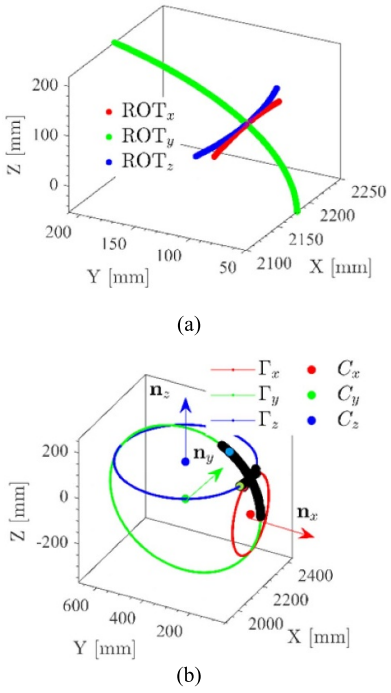

Figure 7. (a) Rotation of hexapod platform about x, y, and z and measured SMR data, (b) calculation of hexapod flange location and vector between flange frame and tool center position frame.

SMR to TCP was computed. This approach enables the translation of laser-tracker measurements into equivalent ballbar measurements. A common coordinate frame of reference is an essential requirement for real-time position compensation. Although any reference frame can be used for this purpose, there are some complications and considerations in its choice.

Robot programming for a circular path is typically based on the assumption of a perfect kinematic model, with positions referenced to the robot's root frame. For the circular path error compensation, the measured compensation values must be applied within the root frame of the robot. This ensures that the process of creating a compensated robot path remains consistent with the standard uncompensated process. Consequently, measurements obtained from the laser tracker must be transformed into the root frame of the robot. In this study, the PAM method [28] was employed. This statistically based technique is commonly used to analyze the distribution of a set of shapes and to determine the optimal rotation and/or reflection (i.e. the optimal orthogonal linear transformation) of one object relative to another. Some successful examples of Procrustes Analysis in coordinate-system translation can be found in [29, 30]. The following algorithm summarizes the steps for applying the PA method in the current study (table 1).

To obtain the rotation and translation matrices from the laser tracker frame to the hexapod base frame, the hexapod flange was guided through a grid-point trajectory within parallel *YZ* planes comprising 238 equally spaced positions over a range of [300, 300, and 200] mm along each axis. The grid points were defined relative to the hexapod base frame, with

Table 1. Algorithm 1 for procrustes analysis.

Algorithm 1. Procrustes Analysis applied to Laser tracker and Hexapod frames.

Require: ${}^{\mathcal{F}_b}\boldsymbol{p}_f \in \mathcal{R}^{N\times 3}$ ▶ nominal flange positions in base frame
$\widetilde{{}^{\mathcal{F}_l}\boldsymbol{p}_s} \in \mathcal{R}^{N\times 3}$ ▶ measured SMR positions in LT frame
${}^{\mathcal{F}_l}\boldsymbol{p}_{sf} \in \mathcal{R}^{1\times 3}$ ▶ offset between flange and SMR
Ensure: ${}^{\mathcal{F}_b}_{\mathcal{F}_l}\boldsymbol{R} \in \mathcal{R}^{3\times 3}$ ▶ rotation matrix from LT to base frame
${}^{\mathcal{F}_b}_{\mathcal{F}_l}\boldsymbol{T} \in \mathcal{R}^{3\times 3}$ ▶ translation matrix from LT to base frame
▶ *Get measured flange positions*
1: $\widetilde{{}^{\mathcal{F}_b}p_f} \leftarrow \widetilde{{}^{\mathcal{F}_l}p_s} - {}^{\mathcal{F}_l}p_{sf}$
▶ *Get centroid of flanges nominal & measured position*
2: ${}^{\hat{\mathcal{F}}_b}p_f \leftarrow mean\left({}^{\mathcal{F}_b}p_f\right) \in \mathcal{R}^{1\times 3}$
$\widetilde{{}^{\tilde{\mathcal{F}}_l}p_f} \leftarrow mean\left(\widetilde{{}^{\mathcal{F}_l}p_f}\right) \in \mathcal{R}^{1\times 3}$
▶ *Get centered flange nominal and measured positions*
3: ${}^{\hat{\mathcal{F}}_b}p_f \leftarrow {}^{\mathcal{F}_b}p_f - {}^{\overline{\mathcal{F}_b}}p_f$
$\widehat{{}^{\mathcal{F}_l}p_f} \leftarrow {}^{\mathcal{F}_l}p_f - \widetilde{{}^{\tilde{\mathcal{F}}}p_f}$
▶ *Get their covariance matrix*
4: $\sum {}^{\mathcal{F}_b}p_f\widetilde{{}^{\mathcal{F}_l}p_f} \leftarrow Cov\left({}^{\mathcal{F}_b}p_f, \widetilde{{}^{\mathcal{F}_l}p_f}\right)$
▶ *Get corresponding Singular Value Decomposition (SVD)*
5: $[\boldsymbol{U}, -, \boldsymbol{V}] \leftarrow SVD\left(\sum {}^{\mathcal{F}_b}p_f\widetilde{{}^{\mathcal{F}_l}p_f}\right)$
▶ *Get optimal rotation matrix between two frames*
6: ${}^{\mathcal{F}_b}_{\mathcal{F}_l}\boldsymbol{R} \leftarrow \boldsymbol{V}\cdot\boldsymbol{U}^T$
▶ *Check if the matrix is a proper rotation*
7: $\det\left({}^{\mathcal{F}_b}_{\mathcal{F}_l}\boldsymbol{R}\right) = 1$
▶ *Correct the reflection issue if required*
8: ***If*** $\det\left({}^{\mathcal{F}_b}_{\mathcal{F}_l}\boldsymbol{R}\right) \prec 0$ ***then***
9: $\boldsymbol{V}[:, end] = -\boldsymbol{V}[:, end]$
10: ${}^{\mathcal{F}_b}_{\mathcal{F}_l}\boldsymbol{R} \leftarrow \boldsymbol{V}\cdot\boldsymbol{U}^T$
▶ *Get optimal translation matrix between two frames*
11: ${}^{\mathcal{F}_b}_{\mathcal{F}_l}\boldsymbol{T} \leftarrow \left(\widehat{{}^{\mathcal{F}_l}p_f}\right)^T - {}^{\mathcal{F}_b}_{\mathcal{F}_l}\boldsymbol{R}\cdot\left(\widehat{{}^{\mathcal{F}_b}p_f}\right)^T$

the *YZ* planes chosen owing to the circular motion of the ballbar occurring in the *YZ* plane without individual axis rotations. The nominal flange position was recorded for each reachable grid point, and the SMR measurement relative to the laser-tracker frame was captured. With knowledge of the offset between the hexapod flange and SMR, the measured flange position was estimated. These nominal and measured values are then used to compute the rotation and translation matrices using algorithm 1.

The following steps were applied to compute the circular path error (figure 8). First, the desired nominal circular path points Pf are generated by the hexapod controller in the hexapod reference frame Fb. For consistency, the circular-path error was evaluated in the *ZX* plane. Given the known offset vector u between the hexapod flange and TCP, the corresponding nominal TCP circular path points Pt are computed.

A 3D least-squares fitting technique was then employed to determine the optimized circular path Γt along with its center and constant radial distance *rt*. Simultaneously, a laser tracker measured the circular path positions of the SMR, denoted as *Ps*. Using the known offset vector v between SMR and TCP, the corresponding measured TCP circular path points, $\tilde{P}t$. The previously derived rotation and translation matrices

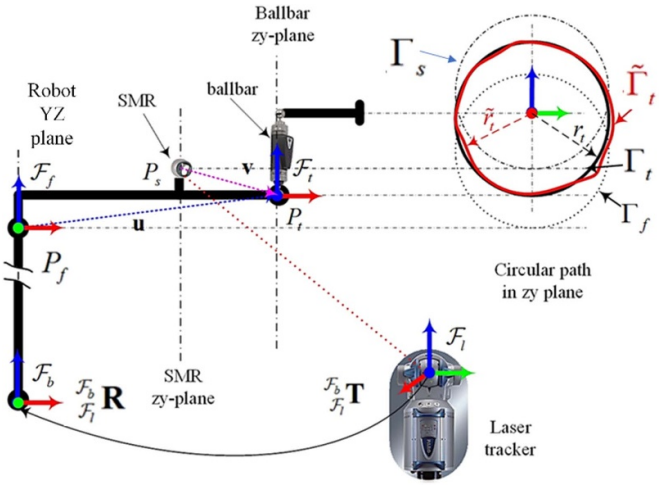

Figure 8. Circular path error calculation process using laser tracker.

between the laser tracker and the hexapod frames were then applied to express the measured TCP positions in the hexapod base frame. Another 3D least-squares fitting was performed to determine the optimized measured circular path $\tilde{\Gamma}\ t$ along with its center and radial distance $\tilde{r}\ t$. The circular path error

was then computed as the difference between the nominal and measured radial distances.

4. Results and analysis

4.1. Effect of compensation factors on path error correction

Successful circular path error compensation necessitates appropriate selection of the sampling rate of the measurement tool, feed speed of the hexapod machining cell, number of control points for the circular path, and circular path radius. When using an offline compensation method, a higher number of control points for a circular path is generally preferred. However, an excessive number of control points can complicate arc motion generation owing to the insufficient time for the robot to accelerate its speed. To address this issue, a series of control points ranging from 180, 360, 720, and 1440-was introduced. For example, 1440 control points correspond to four control points per one-degree arc. Using equation (15) and the corresponding results were calculated (figure 9). A higher sampling rate was required when higher feed rates and greater numbers of control points were selected (figure 9(a)). For a ballbar radius of 50 mm, when 720 control points are required and the feed rate is 1200 mm min^{-1}, the minimum required sampling rate exceeds 45 Hz (figure 9(b)). Under these conditions, the standard ballbar configurations can satisfy these requirements.

To validate the above theoretical results, for the given ballbar with radius of 50 mm, tests were conducted at feed speeds of 1200, 1800, 2400, and 3000 mm min^{-1}, with sampling rates of 50, 100, and 1000 Hz. Figure 10 shows the ballbar results (CDs) before and after circular path error compensation for different setups. Similar compensation results were achieved with sampling rates of 50 and 100 Hz, demonstrating the effectiveness of equation (8). The proposed equation serves as an effective guide for selecting the appropriate sampling rate, feeding speed, and control points for circular-path measurements.

For circular path generation, three methods are available: the P2P, the circular arc motion method, and the circle motion method. Figure 11 reveals the ballbar measurement results generated using the three measurement methods. The generation of a circular path was defined using 720 control points. The ballbar raw data, measured using the three methods, along with the corresponding CDs, are available and similar. Additionally, similar radial error patterns were observed for the measurements obtained in both the CCW and CW directions. Therefore, it can be concluded that circular path generation methods have a minimal effect on path error measurement in the non-machining state. However, this may differ in the machining state, as the dynamics of the robot or acceleration/deceleration vary with machining conditions.

Because the circle-motion-based method uses a minimum of four control points, it is more suitable for online path error compensation and not applicable to offline path error compensation. Therefore, the compensated circular path error of the circular path generated by the circular motion method and

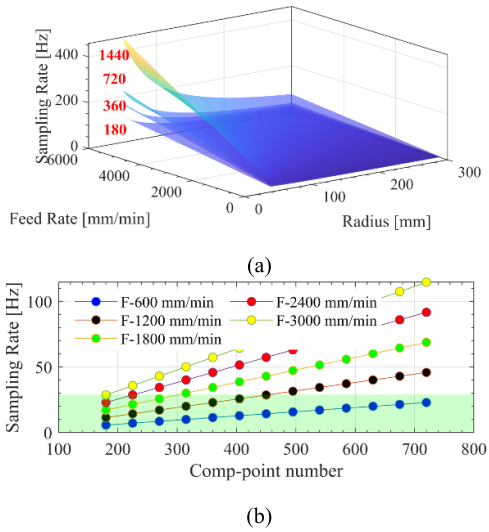

Figure 9. Relationship between the scaling parameter, target function and circular deviations (CDs), and the blue dot of figure (a) stands for the optimal scaling parameter and the light blue plane stands (b) for the control limit (decided by equation (14)) for CD.

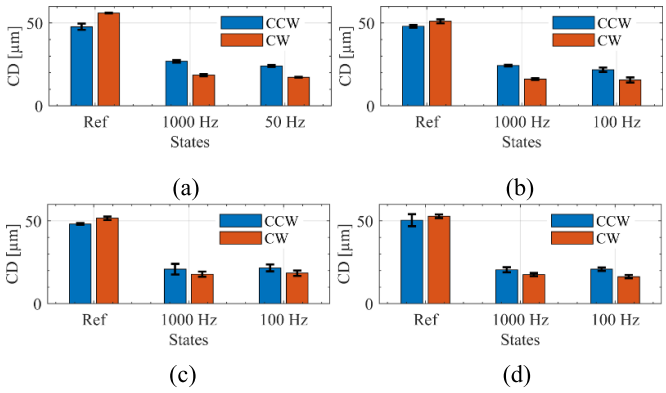

Figure 10. Ballbar results measured before and after compensation at different feeding speeds: (a) 1200 mm min^{-1}; (b) 1800 mm min^{-1}; (c) 2400 mm min^{-1}; (d) 3000 mm min^{-1}.

P2P were compared in this work. For this comparison, different control points for circular path generation were also introduced.

The ballbar raw data obtained before and after path error compensation under varying circular path generation methods are presented in figure 12. Minimal differences were observed between arc numbers of 45 and 90 when employing the arc method. In contrast, significant variances were detected using the P2P method at arc numbers of 45 and 90. When the arc number exceeds 180, fewer differences are observed. However, with the P2P method, only minor variations in each path are detected. For both methods, significant changes in the CDs prior to compensation were observed when the control points were fewer than 180 (figure 13). Similarly, notable differences in the CDs after compensation were evident under the same conditions.

These findings indicate that the arc method exhibits superior performance compared to the P2P method for circular path

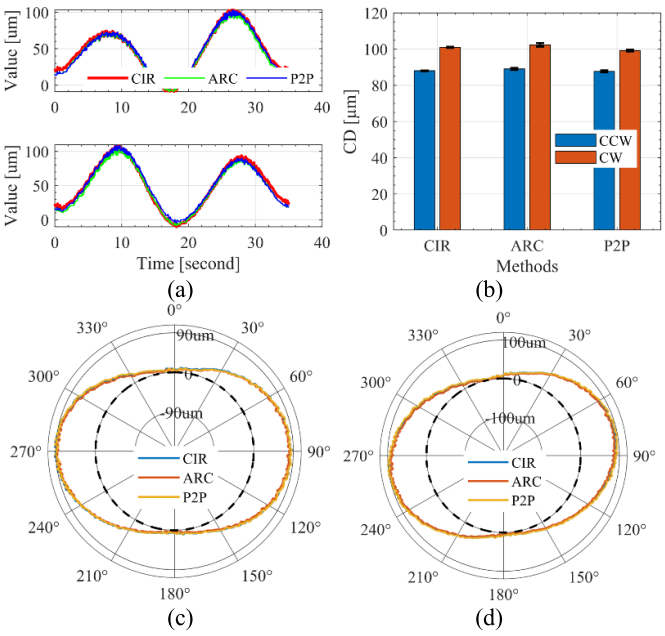

Figure 11. (a) Ballbar raw data measured with three different circular path generation methods; (b) CDs of the circular path generated with three different methods; (c) radial errors of circular path measured with CCW direction; (d) Radial errors of circular path measured with CW direction.

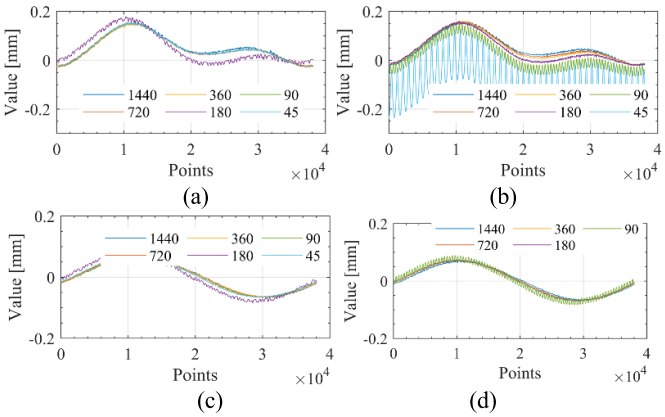

Figure 12. (a) Ballbar raw data measured with the path generated with Arc method before compensation; (b) Ballbar raw data measured with the path generated with P2P method before compensation; (c) ballbar raw data measured with the path generated with Arc method after compensation; (d) ballbar raw data measured with the path generated with P2P method after compensation. Due to the significant path error observed in the circular path generated with 45 points, compensation for this path was excluded.

generation. However, the P2P method achieves a performance comparable to that of the arc method when a larger number of control points is utilized. Consequently, a higher number of control points is recommended for both Arc and P2P methods.

4.2. Effectiveness of ballbar in error measurement and compensation for circular paths with varying radius

A ballbar with a radius of 100 mm, installed at various angles, was employed to measure true radii of 50, 60, 70, 80, 90, and 100 mm. Each measurement was repeated three times to ensure consistency. Figure 14 presents the raw ballbar data before and after path error compensation across different measurement setups. When compared with the raw data obtained at the standard ballbar radius of 100 mm, distinct results were observed for the radius of 50, 60, 70, 80, and 90 mm both before and after error compensation (figure 15). These differences are clearly visible in the path error patterns and the ranges of error values. With respect to radial errors, a pronounced scaling mismatch was identified for the ballbar measured at the standard radius of 100 mm. As the ballbar radius decreased, the radial error shape underwent notable changes, with increasing path errors observed at the points of directional axis changes.

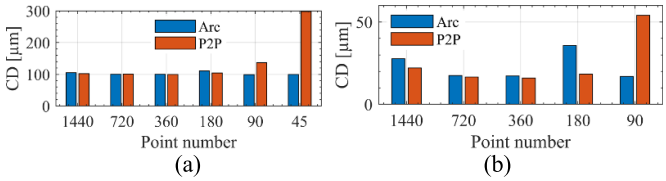

Figure 13. (a) CDs measured at the circular path generated with Arc and P2P methods before compensation; (b) CDs measured at the circular path generated with Arc and P2P methods after compensation.

Following path error compensation, no consistent error patterns were detected; instead, numerous small variations in errors were observed along the circular path.

As for the CDs (figure 16), their measured values decreased with the reduction in the ballbar measurement radius prior to path error compensation, with the minimum CD observed at a measurement radius of 50 mm. Following path-error compensation, the CDs further decreased, with the minimum CD value identified at a ballbar radius of 100 mm. This observation indicates that the effectiveness of the compensation diminishes as the measurement radius decreases.

To quantitatively assess the compensation effect, the compensation rate was calculated. The compensation rate is defined as the ratio of the difference between the CDs before and after path error compensation to the CD BC (figure 16). The lowest compensation rate (16.7%) was observed at a radius of 50 mm, corresponding to a swinging angle of 60 °. This phenomenon is attributed to the errors projected onto the x-axis of the hexapod. Specifically, when the out-of-plane angle exceeded 45°, the errors projected onto the testing plane became smaller than those projected onto the x-axis. Consequently, more path error components were retained on the testing plane, indicating that smaller out-of-plane angles are preferable. Based on this finding, the minimum compensation rate was 44%. Additionally, parameters 35 and 59, indicated in figure 21 were obtained from the laser tracker discussed in the subsequent section. These values represent the minimum CDs BC and maximum CDs after compensation, respectively. Comparable results between the ballbar and laser tracker measurements were obtained when the testing radius was 70 mm. Therefore, the compensation effect of the proposed ballbar measurement was influenced by the out-of-plane

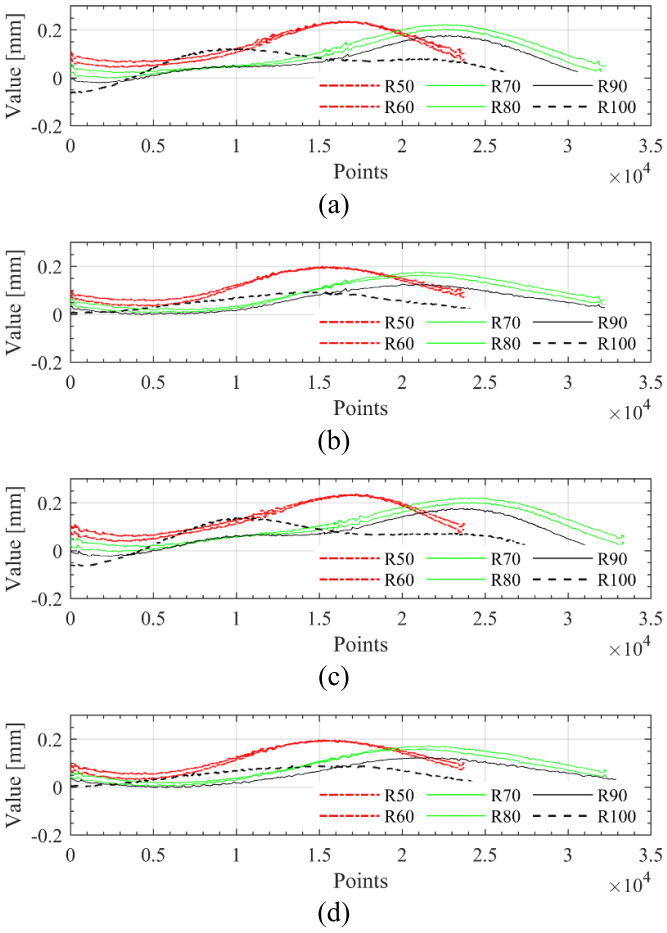

Figure 14. Circular path raw data measured with ballbar at the CCW (a), (b) and CW (c), (d) directions for the radius from 50 to 100 mm before (a), (c) and after (b), (d) path error compensation.

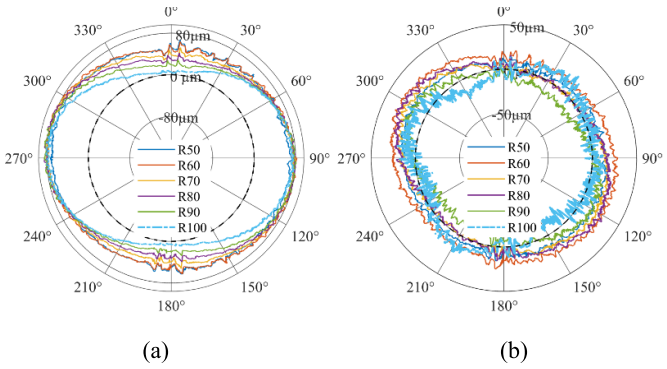

Figure 15. (a) Radial error measured at the CCW direction before path error compensation; (b) radial error measured at the CCW direction after path error compensation.

angle. Optimal compensation can be achieved when the out-of-plane angle is less than 30 °, with the highest level of compensation occurring at smaller out-of-plane angles.

The radial errors measured under different radii and out-of-plane angles exhibit several consistent characteristics. First,

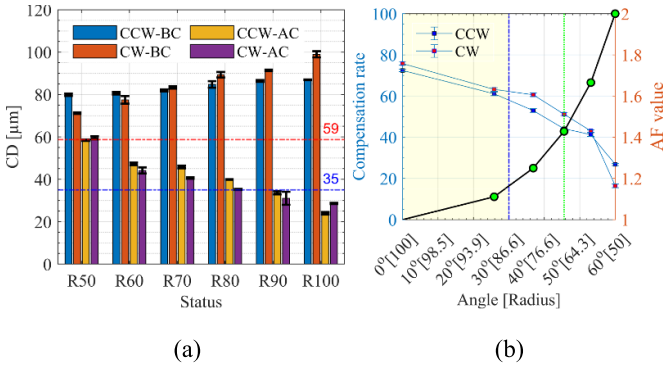

Figure 16. (a) CDs of ballbar before and after path error compensation. BC and AC stand for the before compensation and after compensation (same definition for the next figures); the 59 and 35 stands for the references of the laser tracker which are the minimal value of CDs before compensation and maximum value of CDs after compensation; (b) compensation rate of ballbar and the theoritical analysis of AF parameters under different setups of out-of-plane angles.

the errors show periodic fluctuations along the circular trajectory rather than random noise, which reflects the repeated influence of robot joint accuracy and structural compliance at different angular positions (figures 15 and 19). Second, the error patterns obtained in CW and CCW motions are approximately symmetric, as the underlying space motion errors originate from robot geometry and stiffness rather than motion direction (figure 14). Third, the magnitude of deviations increases when the circular radius decreases or when the out-of-plane angle becomes larger. This trend is clearly visible in the raw data of figure 14 and the CD values in figure 16, and is also consistent with the theoretical projection model in section 2.2, where the AF predicts larger distortions at higher out-of-plane angles. Together, these results provide a clearer description of the typical characteristics of radial errors in circular path motion.

To expand the verification range of the proposed ballbar out-of-plane measurement, an improved small circular adaptor was employed for circular path measurements with radius of 35, 40, 45, 48, 49 and 50 mm. The following (figure 17) reveal the CDs and compensation rate of the ballbar under different radii before and after path error compensation. This measured radius is located in the range of the proposed ballbar out-of-plane angles (less than 30°), and a good compensation result can be found after path error compensation, and a reliable compensation rate can also be found. In addition, similar changes in the ballbar raw data and radial error data as ballbars with a radius of 100 mm were also found.

4.3. Comparison of ballbar and laser tracker on circular path error compensation

During the ballbar measurement process, a laser tracker was concurrently employed to assess the path error of the circular trajectories with radii ranging from 50 to100 mm. The reflective markers were placed at position P2 for these measurements. As P2 was located at a distance from P1, which was

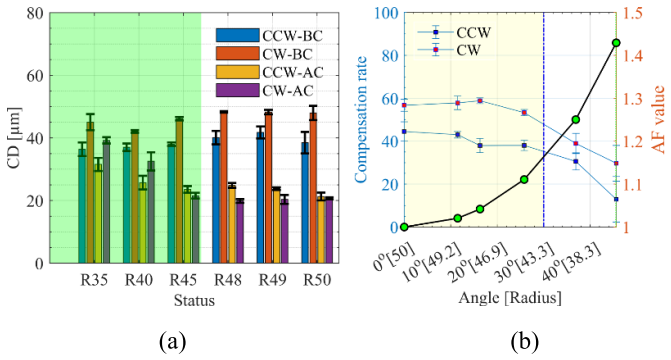

Figure 17. (a) CDs of ballbar before and after path error compensation. The green rectangle stands for the extended measurement range for ballbar with a radius of 50 mm; (b) compensation rate of ballbar and the theoritical analysis of AF parameters under different out-of-plane angles while the yellow rectangle box stands for the recommended range for angular ballbar setup.

connected to one end of the ballbar, discrepancies in the measurement results between the two positions were anticipated. Accordingly, after each test, a laser tracker was used to repeat the measurements at P1 for comparison (figure 18). Similar raw radius data were obtained for the CCW and CW directions at both P1 and P2 positions. Therefore, for the subsequent measurements, the reflective marker was positioned at P2. When compared with the radius raw data obtained from ballbar measurements, the raw data measured by the laser tracker exhibited magnitudes that were approximately 25% smaller. After compensation, a further reduction in the radius of the raw data is observed. In addition, the results from the laser tracker reveal a consistent error pattern. This discrepancy is likely attributed to differences in the data processing methodologies, as the ballbar employs 2D measurements, whereas the laser tracker utilizes 3D measurements.

In the analysis of the radial error distribution, a noticeable scaling mismatch was observed at each measurement radius prior to path error compensation (figure 19). Following compensation, the radial error pattern measured at a radius of 100 mm differed from those observed at other radii. Under identical measurement conditions, the ballbar and laser tracker yielded distinct results, particularly for radii ranging from 50 mm to 90 mm. This discrepancy can be attributed to differences in the raw radius data recorded by the ballbar and the laser tracker. For the ballbar, the initial values for each measurement varied between −0.05 mm and 0.1 mm, whereas the laser tracker exhibited more consistent results, with variations of approximately 0.02 mm. These differences influence the radial error representation when plotted using the Matlab polarplot function.

With respect to the CDs values, a decreasing trend was observed with an increasing ballbar radius (figure 20). The largest and smallest CDs were recorded at radii of 100 mm and 50 mm, respectively. After path-error compensation, the CDs were reduced to a maximum of 35 μm. In terms of the compensation rate, the laser tracker achieved superior results, with a minimum value of 43% compared to the ballbar

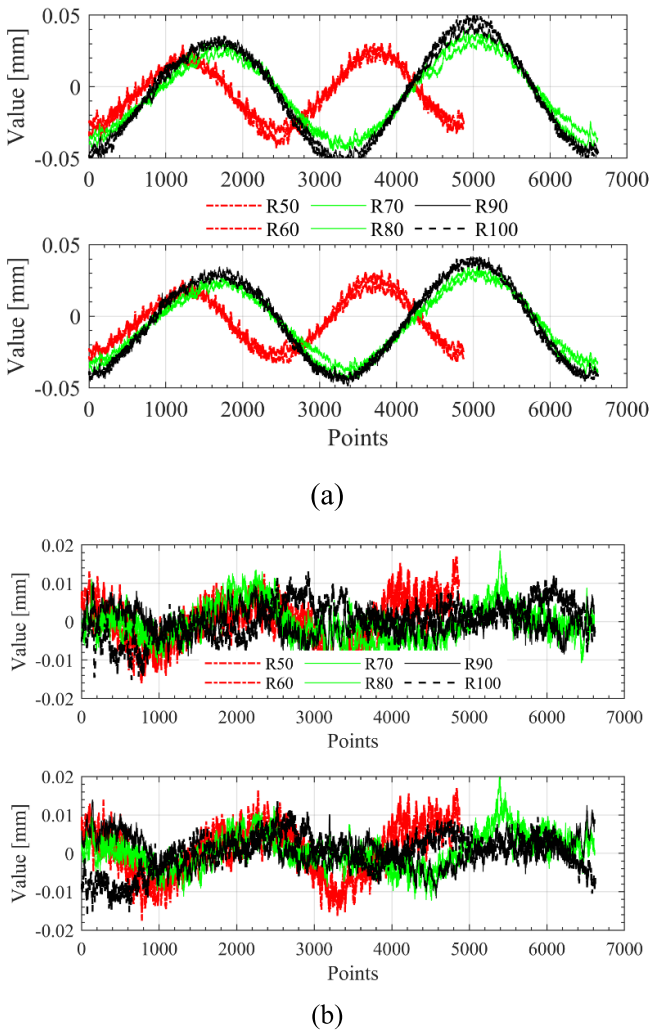

Figure 18. (a) Radial raw data measured with laser tracker at position 1 at different radius before path error compensation; (b) radial raw data measured with laser tracker at position 2 at different radius before path error compensation.

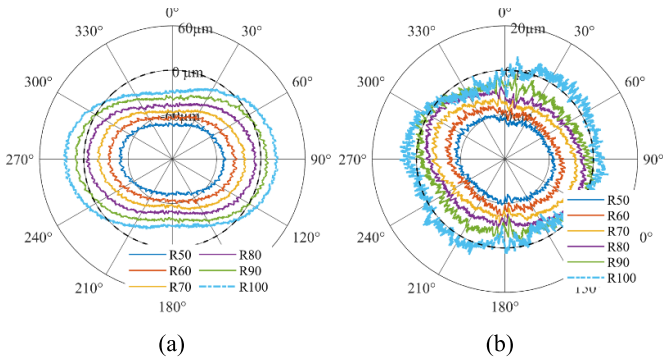

Figure 19. (a) Radial error measured at the CCW direction before path error compensation using laser tracker; (b) radial error measured at the CW direction after path error compensation using laser tracker.

method. Consequently, the laser tracker demonstrated a more effective compensation performance for the CDs than a ballbar equipped with an out-of-plane angle setup.

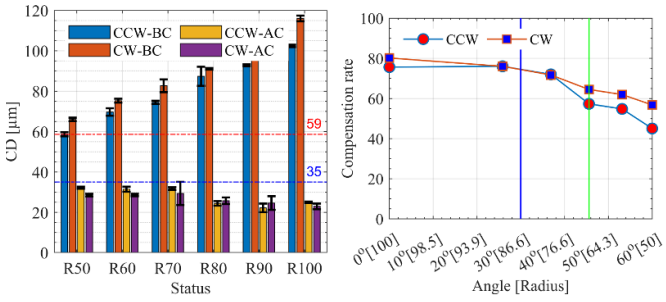

(a) (b)

Figure 20. (a) CDs of ballbar before and after path error compensation; the 59 and 35 stands for the references of the laser tracker which are the minimal value of CDs before compensation and maximum value of CDs after compensation; (b) compensation rate (mean value) of laser tracker under different setups.

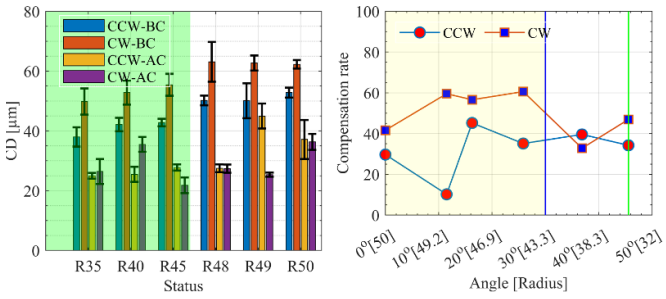

(a) (b)

Figure 21. (a) CDs of laser tracker before and after path error compensation. The green rectangle stands for the extended measurement range for laser tracker with a radius of 50 mm; (b) compensation rate (mean value) of laser tracker under different setups while the yellow rectangle box stands for the recommended range for angular ballbar measurement.

The path error measurement and compensation were performed using a ballbar with a radius of 50 mm in conjunction with a laser tracker. By employing the proposed laser tracker data processing method, the changes in CDs and compensation rates before and after path error compensation were calculated, as illustrated in figure 21. Following the compensation, the CDs were significantly reduced. A relatively stable compensation rate was achieved, and better compensation could be found by the laser tracker at the general measurement radius when compared with the ballbar.

To facilitate a more comprehensive comparison between the ballbar and laser tracker, the results are summarized in the following table (table 2). The comparison focuses on key areas, including the range of raw data variation before and after compensation, radial error curve patterns, CDs and compensation rates, testing complexity, and cost of testing equipment. Firstly, the ballbar measurement was performed on the 2D plane using a 2D least-squares fitting method. By contrast, the laser tracker measures the 3D coordinates of the reflective target and calculates the radial error using a 3D least-squares fitting method. The inclusion of the x-axis, as defined by the research platform, aids in accurately determining the radial error for the circular path. Second, the radial raw data from the ballbar, both before and after path error compensation, tend to be larger than that from the laser tracker. In addition, the range of change in the CDs before path error compensation generally follows this pattern. However, after compensation, the CDs measured by the laser tracker are smaller than those measured by the ballbar. Ultimately, these differences manifest in the compensation rate, where the laser tracker shows a more effective compensation ($\geqslant$57%) than the ballbar ($\geqslant$44%).

Thirdly, the radial error pattern serves as a crucial indicator for identifying the specific machine error parameters. Before path error compensation, the ballbar detects a significant scaling mismatch at a radius of 100 mm, unlike the laser tracker, which exhibits different errors at different radii. After compensation, both the ballbar and laser tracker at 100 mm displayed similar error patterns. However, at other radii, the laser tracker maintained a consistent error pattern, whereas the ballbar did not. This inconsistency is primarily due to the out-of-plane angles of the ballbar, which affect the initial raw data and the method used for calculating path errors. Finally, implementing the ballbar and laser tracker involves different testing procedures for measuring path errors. Compared with the laser tracker, the ballbar requires fewer complex setups. In contrast, the laser tracker requires alignment with the robot using grid point measurements (approximately 238 positions in this study) and additional data processing through Procrustes analysis. This alignment process can take up to 30 min. Moreover, maintaining the stationary position of the

Table 2. Comparison of ballbar and laser tracker in different items using ballbar with the radius of 100 mm.

No.	Items	Ballbar	Laser tracker
1	Fitting method	2D least square fitting (LSF)	3D LST
2	Change range of raw data before/after compensation	−0.06–0.23 mm/0–0.19 mm	−0.05–0.05 mm/−0.02–0.02 mm
3	Change range of CDs before/after compensation	71–98 μm/24–59 μm	59–116 μm/23–35 μm
4	Change range of compensation rate	16%–71%	45%–85%
5	Change range of compensation rate when out-of-plane angle is bigger than 30°	⩾61%	⩾75%
6	Radial error curve patterns before compensation	Not clear, scaling mismatch	Not clear, scaling mismatch
7	Radial error curve patterns after compensation	Clear, scaling mismatch	Clear, scaling mismatch
8	Testing complexity	Simple	Complex
9	Total measurement time	Circular path measurement (CPM)	CPM + coordinate alignment
10	Cost of testing device	0.1–0.2 of *P*	*P*

laser tracker throughout the measurement process is crucial for avoiding unexpected errors. Given the complexity and precision required in the measurement process, operators with high technical skill levels are preferred. Additionally, the laser tracker is significantly more expensive than the ballbar, costing approximately five to ten times more.

The proposed ballbar with an out-of-plane angle measurement demonstrated a performance comparable to that of a laser tracker when the out-of-plane angle was less than 30°. Compared to the standard ballbar configuration, the out-of-plane ballbar measurement extends the application range of ballbars with radii of 50, 100, and 150 mm to other randomly selected radii ranging from 50 to 150 mm. Furthermore, with a relatively simple setup, a compensation rate difference of approximately 10% relative to the laser tracker was achieved. Moreover, compared to the laser tracker, the lower hardware investment required for the ballbar makes it more suitable for shop floor applications in small- and medium-sized enterprises.

5. Discussion and practical implications

In this study, the measurement and compensation of path errors in robotic machining were investigated using a ballbar and a laser tracker. Conventional ball bars are limited to fixed-radius measurements for positioning error assessments or machine tool calibration. To address this limitation, a novel out-of-plane ballbar measurement method, along with a corresponding data processing approach, is proposed. Theoretical analysis and experimental validation of the proposed method were conducted, demonstrating its applicability to variable radius measurements.

To comprehensively present the proposed technology, factors influencing circular path generation, such as sampling rate, feed speed, number of control points, and circular path radius, were analyzed on a hexapod machining cell (FANUC) research platform. The theoretical relationships between these factors were established and validated. The circle motion-based method was found to be more suitable for online path error compensation, but not for offline compensation. Comparative analysis revealed that the arc method outperformed the P2P method in circular path generation. However, the P2P method achieved a performance comparable to that of the arc method when a higher number of control points was employed. Consequently, a higher density of control points is recommended for both methods. The Arc method is more suitable for machining tasks because of its ability to eliminate vibrations during transitions between the control points. In contrast, the P2P method is better suited for applications that require movement along a specific sequence of discrete points, such as pick-and-place operations or inspections involving predefined locations.

The observed characteristics of radial errors can be further interpreted in the context of robot space motion errors. As discussed in section 2.2, space motion errors of industrial robots originate from multiple sources, including geometric deviations, thermal effects, servo control limitations, and structural compliance. The radial errors identified in this study represent the projection of these space motion errors onto the radial direction of circular trajectories. Their periodicity along the path reflects the repetitive influence of joint and link deviations, while the symmetry between CW and CCW motions indicates that the dominant errors are structural rather than direction-dependent. Furthermore, the increase in radial error magnitude at smaller radii and larger out-of-plane angles can be directly explained by the projection model, where distortion grows with the AF (equation (5)). These findings confirm that radial errors not only capture the dominant manifestation of robot space motion errors during circular motion, but also provide a practical target for measurement and compensation using the proposed out-of-plane ballbar method.

After establishing a clear understanding of the relationships among the aforementioned factors, the ballbar and laser tracker were applied for path error measurement and compensation at various radii. Experiments were performed using ballbars with lengths of 100 mm and 50 mm under different out-of-plane angles. A novel small circular adaptor was developed to enable the use of a ballbar with a radius of 50 mm for various radius measurements. This innovation extends the maximum out-of-plane angle of a conventional Renishaw ballbar with a radius of 50 mm from 20°to 45°. Using the proposed data

processing method for the ballbar under various out-of-plane angles, measurements at different radii were calculated and compared in terms of the circular path raw data, radial error patterns, CD, and compensation rates. For a standard measurement radius of 100 mm, the ballbar and laser tracker produced similar results for these metrics. However, under out-of-plane angle conditions, discrepancies between the ballbar and laser tracker results were observed, and these differences increased as the out-of-plane angle increased (corresponding to a decrease in the measurement radius). Although the laser tracker has a lower resolution than the ballbar, it achieves a higher compensation rate (45%–85% vs. 16%–71%). The possible reasons for this are as follows: (1) the ballbar operates in a 2D plane and captures only radial information, whereas the laser tracker performs 3D measurements, allowing it to detect unexpected movements along the vertical direction of the ballbar testing plane. The absence of vertical movement data in ballbar measurements introduces a theoretical limitation in circular path measurement and error compensation. (2) The out-of-plane angle of the ballbar for various radius measurements has limitations in radial error measurement and compensation. For a given measurement position, the true radial error, defined as the difference between the true and nominal radii, can correspond to three possible offset positions. Relying on a single radial error measurement makes it challenging to precisely determine the offset values for the *X*- and *Y*-axes, representing an inherent limitation of the proposed method. In this study, position 1 was used as the reference point to calculate the compensation value. However, this limitation can be mitigated by increasing the number of control points and sampling rate. (3) The calculated radial error projected onto the ballbar measurement plane was used for path-error compensation. The relationship between the radial error components projected onto the ballbar measurement plane and the vertical direction of the plane was influenced by the out-of-plane angles of the ballbar. Ideally, minimizing radial errors in the vertical direction of the ballbar measurement plane is preferred. When the error in the vertical direction becomes significantly larger than that in the measurement plane (e.g. when the out-of-plane angle exceeds 45°), unexpected movements in the measurement may occur. A model-based qualitative decomposition (appendix A2 (table A1)) indicates that the dominant contributors to the gap are the 3D-to-2D projection and axial leakage at non-zero out-of-plane angles, whereas control-point discretization and sampling effects play secondary roles and can be mitigated by increasing N1 and complying with equation (12).

To improve the traceability of measurement errors, we have decomposed the error sources into several categories, including projection distortion, sampling and synchronization effects, adaptor-related errors, robot-induced disturbances, and instrument limitations. While projection distortion becomes dominant at larger out-of-plane angles ($\alpha > 30°$), robot-induced disturbances such as vibration and compliance are closely related to the periodic fluctuations observed in radial error curves. Sampling and synchronization effects primarily influence high feed-rate tests, where insufficient data rates may distort the error profile (see figure 10). Adaptor-related errors are more critical in small-radius experiments due to increased mechanical sensitivity. Instrument limitations define the baseline uncertainty, explaining part of the difference in compensation rates between the ballbar and the laser tracker. A detailed summary of these error sources and their potential influence is provided in appendix A3 (table A2).

Therefore, it is recommended to use the proposed ballbar measurement method with a smaller out-of-plane angle (see appendix A4 (table A3) for a consolidated view of sources, scaling, and mitigation). Although the aforementioned limitation exists, path error compensation achieves a compensation rate exceeding 40% when the out-of-plane angle is less than 30°. In addition, the ballbar accounts for only 10%–20% of the total hardware cost of a laser tracker and requires a simple setup and data processing, making it an effective tool for circular path error compensation.

Although all primary experiments in this study were conducted on a FANUC hexapod machining cell, the proposed compensation framework is essentially kinematics-independent because it relies only on commanded circular trajectories and radial errors measured by the ballbar. To further validate this transferability, we carried out a supplemental experiment on a six-degree-of-freedom FANUC serial industrial robot (LR Mate 200iR) under the same conditions as the hexapod tests The results revealed 60%–70% compensation range on the serial robot, with compensation rate differences within approximately 10%–15% compared to the hexapod (appendix A5). This outcome can be explained by the fact that the compensation procedure operates in the task plane and does not depend on the specific forward/inverse kinematics of the platform. The main factor affecting cross-platform performance is the dynamic compliance in the out-of-plane direction: while serial robots typically have lower rigidity than hexapods, the influence of axial disturbances remains small when the out-of-plane angle is kept below about 30°. Therefore, under recommended setup conditions, the proposed method can be expected to yield comparable compensation rates across both hexapod and serial robot platforms.

To implement the proposed out-of-plane ballbar measurement method, two distinct setups can be used to measure a specific radius, as illustrated in figure 2. The ballbar tip connected to the spindle side represents the cutter, whereas the tip attached to the magnetic assembly serves as the rotation center for the circular path to be machined. To ensure that the measured circular path closely corresponds to the circular path of the tool movement, the out-of-plane angle can be optimized or selected based on the requirements of circular part machining in practical applications. Furthermore, an alternative technical approach for improved path error compensation can be achieved through the structural optimization of the ballbar and its calibration pad. An adjustable ballbar length can be implemented using a telescopic-locking mechanism, allowing length adjustments at defined intervals. By

optimizing the ballbar battery, the minimum ballbar length could be set to 70 mm (using the Renishaw ballbar as an example). In addition, a fixed-length calibration structure can be integrated into a plate, enabling the optimized calibration pad to support six predefined fixed distances. With this optimized ballbar, only a small angular adjustment is required for general circular path measurements, minimizing potential errors. Ultimately, improved path error compensation can be achieved through the optimized ballbar structure and its out-of-plane angle for application on the shop floor. For broader context beyond the laser tracker baseline, we added a concise comparison of representative low-cost tools in appendix A6 (table A4), covering accuracy class, cost, setup complexity, and key pros and cons. Finally, the proposed work occupies a middle ground: it retains sub-micron sensing from the ballbar and supports variable radii for task-plane compensation at low cost, while avoiding the full 3D instrumentation and cost of a tracker.

6. Conclusion and future work

This study investigates offline path error measurement and compensation in robotic machining using a ballbar and a laser tracker. To overcome the limitations of traditional ballbars, which operate only at fixed radii, a novel out-of-plane angle measurement method and corresponding data processing approach were proposed for general circular radius measurements. To extend the maximum angular range of a ballbar with a radius of 50 mm, a novel small circular adaptor was developed. Meanwhile, for a better validation of the proposed technology, the factors for circular path error measurement and compensation, including the sampling rate, feed speed, number of circular path control points, and circular path radius, were explored. A theoretical analysis and experimental validation of the proposed out-of-plane ballbar measurement method and small circular adaptor were conducted, confirming their applicability for variable-radius measurements and path error compensation.

(1) The proposed small circular adaptor extends the ballbar out-of-plane angle range from 20° to 45°, enabling circular path error measurement for radii ranging from 35 mm to 50 mm.
(2) For a given circular path error measurement radius, a higher sampling rate is required when higher feed rates and a larger number of control points are used. Under the optimized ballbar measurement setup, the arc-based, circle-based, and P2P methods yield comparable path error measurement results. However, the arc-based method demonstrates superior robustness compared with the P2P method in path error compensation, particularly when the number of control points is limited.
(3) The proposed out-of-plane ballbar measurement expands the traditional ballbar measurement range for circular-path error measurement and compensation. With an out-of-plane angle below 30°, a compensation rate exceeding 61% can be achieved, which is only 14% lower than that of a laser tracker that supports arbitrary circular radii of movement. However, the ballbar accounts for only 10%–20% of the hardware cost and requires a simpler setup and data processing workflow, highlighting its potential as a practical and economical alternative for shop floor circular path error compensation.

Although the proposed out-of-plane ballbar measurement method achieves an optimized compensation comparable to that of the laser tracker in terms of circular path error compensation, there is still room for improvement in the compensation rate. Further technical enhancements can be realized through the structural optimization of the ballbar and its calibration pad. In addition, future work will focus on applying the proposed ballbar angle setup method to real-world scenarios of circular path error compensation. Moreover, the method of combining the proposed out-of-plane ballbar measurement and online path error compensation for FANUC using the DPM function is also explored.

Data availability statement

The data cannot be made publicly available upon publication because they contain commercially sensitive information. The data that support the findings of this study are available upon reasonable request from the authors.

Acknowledgments

The financial support provided by the Fonds de recherche du Québec-Nature et Technologies (FRQNT) through a postdoctoral research scholarship (2023–2024), as well as by the Natural Sciences and Engineering Research Council of Canada (NSERC), is gratefully acknowledged.

Author contributions

Kanglin Xing
Conceptualization (lead), Data curation (lead), Investigation (lead), Methodology (lead), Software (lead), Validation (lead), Visualization (lead), Writing – original draft (lead), Writing – review & editing (equal)

Yannick Cianyi 0000-0002-7827-5819
Conceptualization (equal), Data curation (equal), Investigation (equal), Methodology (equal), Software (equal), Visualization (equal), Writing – original draft (equal)

Ilian A Bonev 0000-0002-9663-2496
Conceptualization (equal), Funding acquisition (equal), Investigation (equal), Project administration (equal), Supervision (equal), Writing – review & editing (equal)

Henri Champliaud 0000-0003-4486-6204
Conceptualization (equal), Funding acquisition (equal), Investigation (equal), Methodology (equal), Project administration (equal), Supervision (equal), Writing – review & editing (equal)

Zhaoheng Liu 0000-0002-8088-7136
Conceptualization (equal), Funding acquisition (equal), Investigation (equal), Project administration (equal), Supervision (equal), Writing – review & editing (equal)

Appendix A1. Derivation of angle-induced error terms (*YZ* plane, *X*-axis normal)

A.1.1. Nomenclature

To improve clarity, table A1 provides a summary of the main symbols used in appendix A1.

Table A1. Nomenclature for appendix A.

Category	Symbol	Definition
Basic quantities	R	Nominal circular path radius
	m_0	Nominal ballbar length
	α	Out-of-plane angle of the ballbar
	θ	Sampling angle
	μ_{a}	Unit vector of the ballbar axis at angle α
Measurement/reconstruction	m	Measured ballbar length
	$\Delta m = m - m_0$	Increment in ballbar length (raw measurement, before projection correction)
	Δm_{bias}	Measured increment including static bias (e.g. adaptor clearance, joint tolerance)
	$\hat{r}$	Reconstructed radial error after projection correction
	Δ_{r}	Residual radial reconstruction error
Error components/disturbances	r	True radial error component (in-plane)
	t	True tangential error component (in-plane)
	ΔX	Out-of-plane deviation (axial offset along ballbar normal)
	δ	Static bias term (adaptor clearance, joint/socket boundary)
	ε	Random noise or synchronization error
Higher order/additional terms	$\mathcal{O}()$	Higher-order terms relevant for small-radius or high-precision cases
	$K_{\mathrm{eff}}(\alpha)$	Posture-dependent effective stiffness
	F	External load (gravity, machining, or inertial force)

A.1.2. Notation and geometric setup

The nominal circular path lies on the *YZ*-plane. Let e_{r} (radial, in-plane), e_{t} (tangential, in-plane), and e_x (out-of-plane, along the *X*-axis) form an orthonormal triad. At a sampling angle θ, the nominal point is $p_0(\theta)$, the base point of the ballbar is c, and the

nominal ballbar vector is with length $m_0 = \|v_0\| \approx \mathrm{R}$. The ballbar unit direction at out-of-plane angle α is

$$u_\alpha = \cos\alpha\, e_\mathrm{r} + \sin\alpha\, e_x. \tag{A1}$$

Small deviations are decomposed as

$$\delta_\mathrm{p} = r\, e_\mathrm{r} + t\, e_\mathrm{t} + \Delta X\, e_x,\ |r|, |t|, |\Delta X| \ll R \tag{A2}$$

where r equals the in-plane radial error PE_{ra} and ΔX is the out-of-plane (axial) deviation; ε denotes measurement/timing noise.

In addition, δ stands for quasi-static bias (e.g. adaptor clearance, joint/socket boundary); m and m0 stand for measured and nominal ballbar length; Δm stands for measured increment in ballbar length and Δ_r stands for reconstruction error in the radial direction after projection correction.

A.1.3. Linearization of the measured distance

The measured length is $\boldsymbol{m} = \|\boldsymbol{v}_0 + \boldsymbol{\delta p}\|$. A first-order expansion around $\boldsymbol{v}_0$ gives

$$\boldsymbol{m} \approx \boldsymbol{m}_0 + \boldsymbol{u}_{\boldsymbol{\alpha}}^{\top}\, \boldsymbol{\delta p} = \boldsymbol{m}_0 + \boldsymbol{r}\cos\boldsymbol{\alpha} + \boldsymbol{\Delta X}\sin\boldsymbol{\alpha} + \boldsymbol{\varepsilon}. \tag{A3}$$

Hence the measured increment

$$\boldsymbol{\Delta m} = \boldsymbol{m} - \boldsymbol{m}_0 \approx \boldsymbol{r}\cos\alpha + \boldsymbol{\Delta X}\sin\alpha + \boldsymbol{\varepsilon}. \tag{A4}$$

To be mentioned, Δm is the raw increment in ballbar length, not yet corrected for projection.

A.1.4. Radial reconstruction and error decomposition

Following the geometric projection used in the paper (AF), the radial component is reconstructed by

$$\widehat{\boldsymbol{r}} = \frac{\boldsymbol{\Delta m}}{\cos\boldsymbol{\alpha}}. \tag{A5}$$

The reconstruction error along the radial direction is therefore

$$\Delta_r = \widehat{\mathrm{PE}_{ra}} - \mathrm{PE}_{ra} \approx \Delta x \cdot \tan\alpha + \frac{\varepsilon}{\cos\alpha}. \tag{A6}$$

This shows two angle-dependent channels: cross-axis contamination $\boldsymbol{\Delta x}\cdot\tan\boldsymbol{\alpha}$ and projection amplification $\frac{\boldsymbol{\varepsilon}}{\boldsymbol{\cos\alpha}}$.

For a small quasi-static offset $\boldsymbol{\delta}$ on the ballbar axis (e.g. adaptor clearance, joint/socket boundary) adds an axial bias to the measured increment:

$$\boldsymbol{\Delta m}_\mathrm{bias} = \boldsymbol{\Delta m} + \boldsymbol{\delta}. \tag{A7}$$

Note that $\boldsymbol{\Delta m}$ denotes the measured ballbar length increment, whereas $\boldsymbol{\Delta r}$ denotes the scalar reconstruction error along the radial direction. In addition, $\boldsymbol{\Delta m}_\mathrm{bias}$ denotes the actual measured increment including the static bias.

After radial reconstruction (AF), we can get

$$\boldsymbol{\Delta}_\mathrm{r} \approx \boldsymbol{\Delta x}\cdot\tan\boldsymbol{\alpha} + \frac{\boldsymbol{\varepsilon}}{\boldsymbol{\cos\alpha}} + \frac{\boldsymbol{\delta}}{\boldsymbol{\cos\alpha}}. \tag{A8}$$

From equation (A8), even a few microns of δ can be amplified by AF. This formulation shows that even a few microns of $\boldsymbol{\delta}$ can be significantly amplified by AF, especially at large out-of-plane angles. Therefore, ensuring mechanical stability of joints and adaptors is critical for reliable measurements.

A.1.5. Second-order terms and useful bounds

The first-order linearization (equations (A3)–(A6)) already captures the main error channels. However, when the circular radius becomes small or when higher precision is required, second-order contributions may no longer be negligible. To evaluate their influence, we expand the norm to the second order

$$\boldsymbol{m} \approx \boldsymbol{m}_0 + \boldsymbol{u}_{\boldsymbol{\alpha}}^{\top}\,\boldsymbol{\delta p} + \frac{1}{2\boldsymbol{m}_0}(\|\boldsymbol{\delta p}\|^2 - \left(\boldsymbol{u}_{\boldsymbol{\alpha}}^{\top}\,\boldsymbol{\delta p}\right)^2). \tag{A9}$$

So that

$$\boldsymbol{\Delta m} \approx \boldsymbol{r}\cos\boldsymbol{\alpha} + \boldsymbol{\Delta X}\sin\boldsymbol{\alpha} + \frac{1}{2\boldsymbol{m}_0}\left(\boldsymbol{r}^2 + \boldsymbol{t}^2 + (\boldsymbol{\Delta X})^2 - (\boldsymbol{r}\cos\boldsymbol{\alpha} + \boldsymbol{\Delta X}\sin\boldsymbol{\alpha})^2\right). \tag{A10}$$

After division by $\cos\boldsymbol{\alpha}$

$$\widehat{\boldsymbol{r}} \approx \boldsymbol{r} + \boldsymbol{\Delta X}\tan\boldsymbol{\alpha} + \frac{\varepsilon}{\cos\boldsymbol{\alpha}} + \frac{1}{2\boldsymbol{m}_0\cos\boldsymbol{\alpha}}\left(\boldsymbol{r}^2 + \boldsymbol{t}^2 + (\boldsymbol{\Delta X})^2 - (\boldsymbol{r}\cos\boldsymbol{\alpha} + \boldsymbol{\Delta X}\sin\boldsymbol{\alpha})^2\right). \tag{A11}$$

Hence

$$\boldsymbol{\Delta}_{\boldsymbol{r}} \approx \boldsymbol{\Delta X}\tan\boldsymbol{\alpha} + \frac{\varepsilon}{\cos\boldsymbol{\alpha}} + \mathcal{O}\left(\frac{\boldsymbol{r}^2 + \boldsymbol{t}^2 + (\boldsymbol{\Delta X})^2}{\boldsymbol{m}_0\cos\boldsymbol{\alpha}}\right). \tag{A12}$$

Therefore, the second-order contribution is generally negligible for standard robotic machining conditions, but may become noticeable for very small-radius paths or in high-precision tasks.

A.1.6. Small misalignment of the ballbar direction

In addition to out-of-plane inclination α, the ballbar may suffer from a small misalignment toward the tangential direction e_{t}. If the ballbar direction departs slightly toward $\boldsymbol{e}_{\mathrm{t}}$ by a small angle β,

$$\widetilde{\boldsymbol{u}}_{\boldsymbol{\alpha},\boldsymbol{\beta}} \approx \cos\boldsymbol{\alpha}\cos\boldsymbol{\beta}\boldsymbol{e}_{\boldsymbol{r}} + \sin\boldsymbol{\beta}\boldsymbol{e}_{\boldsymbol{t}} + \sin\boldsymbol{\alpha}\cos\boldsymbol{\beta}\boldsymbol{e}_{\boldsymbol{x}}. \tag{A13}$$

Then

$$\boldsymbol{\Delta m} \approx \boldsymbol{r}\cos\boldsymbol{\alpha}\cos\boldsymbol{\beta} + \boldsymbol{t}\sin\boldsymbol{\beta} + \boldsymbol{\Delta X}\sin\boldsymbol{\alpha}\cos\boldsymbol{\beta} + \varepsilon. \tag{A14}$$

And reconstructing with $\cos\boldsymbol{\alpha}\cos\boldsymbol{\beta}$ gives

$$\hat{\boldsymbol{r}} - \boldsymbol{r} \approx \boldsymbol{\Delta X}\cdot\tan\boldsymbol{\alpha} + \boldsymbol{t}\cdot\tan\boldsymbol{\beta} + \frac{\varepsilon}{\cos\boldsymbol{\alpha}\cos\boldsymbol{\beta}}. \tag{A15}$$

For typical fixtures $|\boldsymbol{\beta}| \ll 1^{\circ}$, the $\boldsymbol{t}\cdot\tan\boldsymbol{\beta}$ term is negligible.

A.1.7. Posture-dependent stiffness link.

Out-of-plane deviations can also be influenced by the robot's effective stiffness. If F denotes the external load (gravity, machining, or inertial forces) and $\boldsymbol{K}_{\mathbf{eff}}(\alpha)$ is the effective stiffness at angle α, the axial deviation is approximated by $\boldsymbol{\Delta X} \approx \frac{\boldsymbol{F}}{\boldsymbol{K}_{\mathrm{eff}}(\boldsymbol{\alpha})}$. Substituting into equation (A6), we obtain

$$\boldsymbol{\Delta}_{\mathrm{r}} \approx \frac{\boldsymbol{F}}{\boldsymbol{K}_{\mathrm{eff}}(\alpha)}\tan\alpha + \frac{\varepsilon}{\cos\alpha}. \tag{A16}$$

This equation shows that reduced stiffness at large α further magnifies the $\boldsymbol{\Delta x}\cdot\tan\boldsymbol{\alpha}$ pathway.

A.1.8. Takeaways and validity range

Equations (A6)–(A16) justify the observed knee beyond $\alpha \approx 30^{\circ}$: both $\tan\alpha$ and $1/\cos\boldsymbol{\alpha}$ rise rapidly, and any stiffness reduction increases. The derivation assumes $|\boldsymbol{r}|$, $|\boldsymbol{t}|$, $\boldsymbol{\Delta x} \ll R$ and small misalignment $|\boldsymbol{r}| \ll 1$ rad; under these conditions the second-order remainder (equation (A12)) is negligible.

Appendix A2. Qualitative decomposition of the compensation-rate gap

To interpret the difference between the tracker-based compensation rate (around 75%) and the ballbar-based rate (around 61%), table A2 presents a qualitative decomposition grounded in the projection model of section 2.2 and the compensation procedure in equations (10)–(14). It identifies the governing mechanisms, outlines their sensitivity to out-of-plane angle, control-point density, and sampling rate, and lists practical mitigations.

Table A2. Qualitative decomposition of the compensation-rate gap.

Cause	Qualitative impact on compensation rate	Sensitivity	Mitigation
3D $\rightarrow$ 2D projection	Removes out-of-plane components and distorts in-plane magnitude; reduces effective recoverable error	Increases with α	Keep $\alpha \leqslant 30^{\circ}$, use task-plane evaluation
Axial leakage (cross-axis contamination)	Injects axial disturbances into the radial channel, lowering usable signal	Increases with α and axial vibration level	Reduce α; speed/junction smoothing; stiffness improvement
Control-point discretization	Misses high-frequency components; under-fits local deviations	Decreases as N1 increases	Increase N1; prefer arc-based smooth trajectories
Sampling/instrumentation	Averaging instability if samples per interval are low; noise leaks into PE_r	Decreases with higher rate and stable signal-to-noise ratio	Satisfy equation (12); ensure stable 1000 Hz stream and proper filtering

Appendix A3. Summary of measurement error sources

This appendix provides a detailed breakdown of the error sources that may influence circular path measurements in robotic machining. These errors originate from both the measurement setup and the robot system itself. Table A3 summarizes the main categories of error sources together with their potential influence on the results.

Table A3. Sources of measurement errors in circular path experiments and their potential influence.

Error source	Description	Potential influence on results
Projection distortion	Geometric distortion introduced by the out-of-plane angle (AF $= 1/\cos\alpha$)	Amplification of radial error, especially when $\alpha > 30^{\circ}$
Sampling/synchronization error	Mismatch between robot motion commands and ballbar sampling (1000 Hz)	Phase shift or loss of accuracy in radial error patterns
Small-radius adaptor error	Mechanical tolerance and stability of the custom adaptor	Local offsets or reduced repeatability in small-radius tests
Robot-induced disturbances	Vibrations, structural compliance, servo noise during motion	Periodic fluctuations and additional noise in radial error data
Instrument limitations	Ballbar resolution (0.1 μm), repeatability ($\pm$0.5 μm); laser tracker accuracy (10–30 μm)	Baseline uncertainty, limits in compensation accuracy

Appendix A4. Angle dependence and diagnostics

Building on section. 2.2 and the derivations in appendix A1, this appendix summarizes how each distortion source scales with the out-of-plane angle α. Table A4 lists, for each source, the mechanism term, its angle dependence, and practical mitigation. For consistency with the *yz*-plane convention, out-of-plane deviations are denoted ΔX (along the *X*-axis).

Table A4. Angle dependence of distortion sources and diagnostics.

Source	Mechanism term	Angle scaling	Mitigation
Axial deviations (vibration/compliance)	$\Delta x \cdot \tan\alpha$	$\tan\alpha$	Stiffer pose, damping
In-plane noise, timing mismatch	$\varepsilon/\cos\alpha$	$1/\cos\alpha$	Better sync/filtering
Posture-dependent stiffness	$\Delta X \approx \frac{F}{K_{\text{eff}}(\alpha)}$	Keff↓ with α	Pose planning
Adaptor/joint boundary	$\delta/\cos\alpha$	$1/\cos\alpha$	Tolerances, lubrication

Appendix A5. Out-of-plane ballbar measurement conducted on FANUC serial robot

To assess the transferability of the proposed offline compensation method, supplemental experiments were performed on a six-degree-of-freedom FANUC serial robot (FANUC LR Mate 200iR, figure A1(a)) under conditions comparable to those used on the hexapod platform (circular path radius 50 mm, feed speed 1200 mm min^{-1}, CW trajectory, 720 control points). For ballbar measurement on each radius, three measurements were conducted.

Figure A1(b) shows the ballbar raw signals of the serial robot in the CW direction for radii R50, R49, R48, and R45 (suffix '-a/-b'). The traces exhibit a dominant periodic component with consistent phase across repetitions, indicating structure-driven errors rather than random noise. As the effective out-of-plane angle increases when the tested radius becomes smaller, the peak-to-peak amplitude grows and the curve shows stronger low-frequency undulation, which is consistent with angle-induced projection effects and axial leakage. Figure A1(c) summarizes CDs BC (BC, blue) and after compensation (AC, orange). Across R50–R45, BC values are roughly in the 486.4–541.3 μm range, while AC decreases to about 145.7–197.9 μm with small error bars, showing good repeatability. This corresponds to compensation rates on the order of 60%–71.8% for most radii. Figure A1(d) presents the compensation rate as a function of the out-of-plane angle α (the bracketed number indicates the corresponding measured radius). The trend is monotonic: performance is highest around $\alpha \approx 10°$ and decays as α increases toward 30°, where the rate approaches about 59.3%. This angle sensitivity agrees with the projection analysis in the main text, where larger α both amplifies in-plane distortion and injects more axial disturbance into the radial channel. Practically, maintaining $\alpha \leqslant 30°$ preserves a stable 60%–70% compensation range on the serial robot, which is within roughly 10%–15% of the hexapod results under comparable settings.

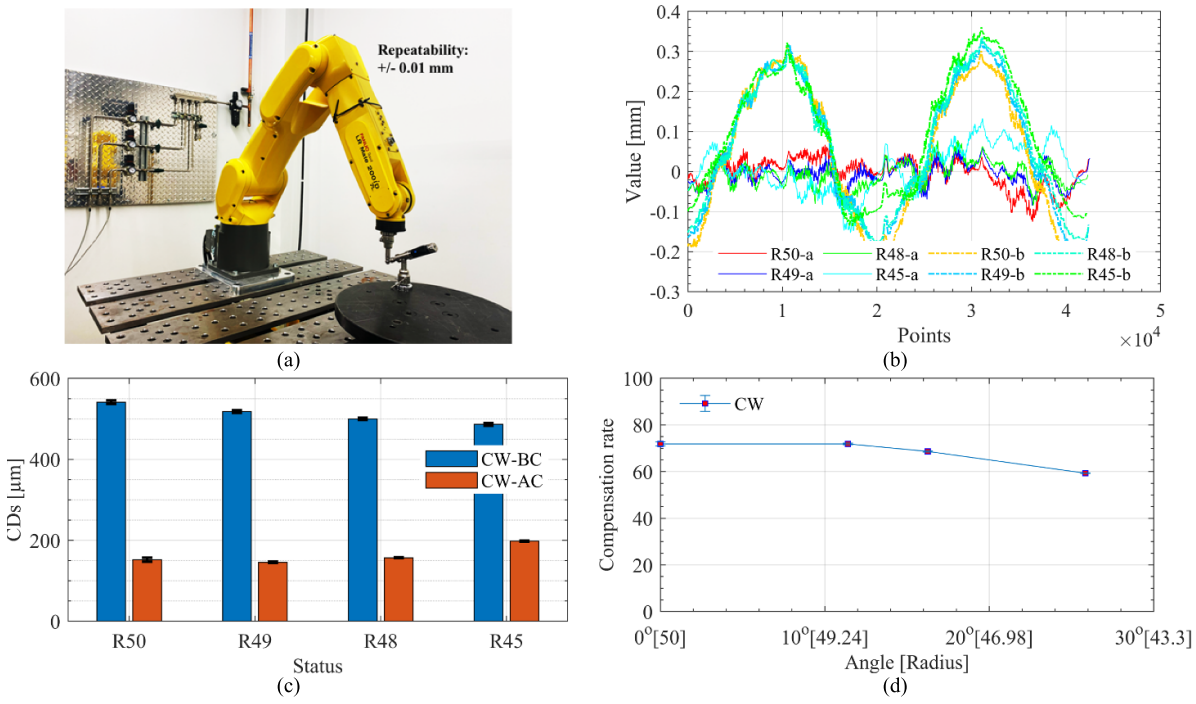

Figure A1. Ballbar measurement with the radius of 50 mm and its measurement results conducted on the FANUC serial rebot (LR Mate 200iR), (a) experimental setup of the FANUC serial robot with out-of-plane ballbar measurement; (b) ballbar raw data of the serial robot in the clockwise (CW) direction at R50, R49, R48, and R45. For each radius, '-b' indicates before compensation and '-a' indicates after compensation; (c) circular deviations (CDs) before (BC) and after (AC) compensation at different radii; (d) compensation rate of out-of-plane ballbar measurements as a function of out-of-plane angle α; bracketed numbers correspond to the measured radius.

The ballbar measurement results demonstrate that the compensation procedure effectively corrects the dominant radial error components independent of robot architecture. These findings further confirm that the proposed out-of-plane ballbar method is applicable not only to parallel hexapod systems but also to conventional serial robots, provided the out-of-plane angle is kept below 30° to minimize axial disturbances.

Appendix A6. Contextual comparison of low-cost circular-path assessment tools

This appendix positions the proposed out-of-plane ballbar approach among representative low-cost options that are commonly considered for shop-floor path evaluation. Table A5 summarizes sensing dimension, typical accuracy class, dynamic suitability, setup complexity, indicative cost level, and key pros and cons. Values are order-of-magnitude estimates synthesized from representative sources and common practice. They serve as background context rather than brand-specific benchmarks.

Table A5. Representative tools for circular-path assessment and compensation context.

Method (representative)	Sensing dimension	Typical accuracy class	Dynamic suitability	Setup complexity	Indicative cost level	Main pros	Main cons
Proposed out-of-plane ballbar	2D radial in the task plane; variable radius via adaptor	Sub-micron sensor resolution; few-micron effective circular-path error for $\alpha \leqslant 30^{\circ}$	High (1000 Hz)	Moderate	Low to medium	Variable radii; fast cycle; direct link to compensation	Sensitive to out-of-plane angle and axial disturbances; 2D projection
LVDT contact displacement + simple center fixture	1D radial displacement along the radius	Micron-level	Medium	Low	Low	Low price; stable; Non sensitive to lighting	Contact friction and speed limits; requires a reliable circle-center reference
Single-point laser triangulation + center fixture	1D radial displacement	Micron to tens-of-microns class	Medium to high	Medium	Low to medium	Non-contact; higher bandwidth	Sensitive to surface reflectivity and incidence angle
Capacitive or eddy-current displacement + metal target	1D near-field displacement	Sub-micron to micron class (short range)	Medium	Medium	Medium	High precision; high bandwidth	Short range; requires metal target or close standoff
Camera with AprilTag fiducials	2D or pseudo-3D image space	Tens-of-microns to several tens-of-microns class	Medium	Medium	Very low	Low-cost hardware; large field of view	Sensitive to calibration and lighting

References

[1] Shi G, Zhao S and Hu B 2020 A practical method to improve absolute positioning accuracy of industrial robot *J. Phys.: Conf. Ser.* **1453** 012121

[2] Jang J H, Kim S H and Kwak Y K 2001 Calibration of geometric and non-geometric errors of an industrial robot *Robotica* **19** 311–21

[3] Li R, Ding N, Zhao Y and Liu H 2023 Real-time trajectory position error compensation technology of industrial robot *Measurement* **208** 112418

[4] Holden R, Lightowler P and Andreou S 2014 Robot accuracy: offline compensation (EU COMET project) *SAE Int. J. Aerosp.* **7** 269–73

[5] Verl A, Valente A, Melkote S, Brecher C, Ozturk E and Tunc L T 2019 Robots in machining *CIRP Ann.-Manuf. Technol.* **68** 799–822

[6] Du G, Liang Y, Li C, Liu P X and Li D 2020 Online robot kinematic calibration using hybrid filter with multiple sensors *IEEE Trans. Instrum. Meas.* **69** 7092–107

[7] Sigron P, Aschwanden I and Bambach M 2023 Compensation of geometric, backlash, and thermal drift errors using a universal industrial robot model *IEEE Trans. on Automation Science and Engineering* pp 1–13

[8] Liu Y, Zhuang Z and Li Y 2022 Closed-loop kinematic calibration of robots using a six-point measuring device *IEEE Trans. Instrum. Meas.* **71** 1–12

[9] Wang Z, Zhang R and Keogh P 2020 Real-time laser tracker compensation of robotic drilling and machining *J. Manuf. Mater. Process.* **4** 79

[10] Möller C, Schmidt H C, Koch P, Böhlmann C, Kothe S-M, Wollnack J and Hintze W 2017 Machining of large scaled CFRP-Parts with mobile CNC-based robotic system in aerospace industry *Proc. Manuf.* **14** 17–29

[11] Ferrarini S, Bilancia P, Raffaeli R, Peruzzini M and Pellicciari M 2024 A method for the assessment and compensation of positioning errors in industrial robots *Robot. Comput.-Integr. Manuf.* **85** 102622
[12] Shu T, Gharaaty S, Xie W, Joubair A and Bonev I A 2018 Dynamic path tracking of industrial robots with high accuracy using photogrammetry sensor *IEEE/ASME Trans. Mechatronics* **23** 1159–70
[13] Gharaaty S, Shu T, Joubair A, Xie W F and Bonev I A 2018 Online pose correction of an industrial robot using an optical coordinate measure machine system *Int. J. Adv. Robot. Syst.* **15** 1729881418787915
[14] Chiwande S N and Ohol S S 2021 Comparative need analysis of industrial robot calibration methodologies *IOP Conf. Ser.: Mater. Sci. Eng.* **1012** 012009
[15] Lou Z, Zhou J, Zhang J, Li W and Fan K-C 2024 Drilling errors compensation of industrial robot based on 3D passive scale tracker *Meas. Sci. Technol.* **35** 095006
[16] Chen D, Yuan P, Wang T, Ying C and Tang H 2018 A compensation method based on error similarity and error correlation to enhance the position accuracy of an aviation drilling robot *Meas. Sci. Technol.* **29** 085011
[17] Nubiola A and Bonev I A 2014 Absolute robot calibration with a single telescoping ballbar *Precis. Eng.* **38** 472–80
[18] Xing K, Bonev I A, Liu Z and Champliaud H 2024 Application of Taguchi method in optimizing the positioning accuracy measurement using helical path ballbar test *Int. J. Adv. Manuf. Technol.* **134** 6019–32
[19] Xing K, Bonev I A, Liu Z and Champliaud H 2024 Influence of machining parameters on dynamic errors in a hexapod machining cell *Int. J. Adv. Manuf. Technol.* **131** 1317–34
[20] Xing K, Bonev I A, Liu Z and Champliaud H 2024 Positioning performance of a hexapod machining cell under machining and nonmachining operations *J. Mech. Sci. Tech.* **38** 6205–24
[21] Rossi C and Savino S 2013 Robot trajectory planning by assigning positions and tangential velocities *Robot. Comput.-Integr. Manuf.* **29** 139–56
[22] Nagata F, Okada Y, Otsuka A, Ikeda T, Kusano T and Watanabe K (eds) 2017 Post processor for industrial robots—circular arc interpolation of CLS data to generate FANUC robotic program *2017 IEEE Int. Conf. on Mechatronics and Automation (ICMA)* (*6–9 August 2017*)
[23] Gattringer H, Mueller A, Oberherber M and Kaserer D 2022 Time-optimal robotic manipulation on a predefined path of loosely placed objects: modeling and experiment *Mechatronics* **84** 102753
[24] Somlo J and Loginov A (eds) 1997 Energetically optimal cruising motion of robots. *Proc. IEEE Int. Conf. on Intelligent Engineering Systems* (*17 September 1997*)
[25] Kelekci E and Kizir S 2023 A novel tool path planning and feedrate scheduling algorithm for point to point linear and circular motions of CNC-milling machines *J. Manuf. Process.* **95** 53–67
[26] Broquere X, Sidobre D and Herrera-Aguilar I (eds) 2008 Soft motion trajectory planner for service manipulator robot *2008 IEEE/RSJ Int. Conf. on Intelligent Robots and Systems* (IEEE)
[27] Conte J, Majarena A C, Aguado S, Acero R and Santolaria J 2016 Calibration strategies of laser trackers based on network measurements *Int. J. Adv. Manuf. Technol.* **83** 1161–70
[28] Schönemann P H 1966 A generalized solution of the orthogonal procrustes problem *Psychometrika* **31** 1–10
[29] Gao X, Yun C, Jin H and Gao Y (eds) 2016 Calibration method of robot base frame using procrustes analysis *2016 Asia-Pacific Conf. on Intelligent Robot Systems (ACIRS)* (*20–22 July 2016*)
[30] Xiaoshan Gao G W, Yun C and Hao D 2017 A calibration method of robot base frame with procrustes analysis *J. Harbin Inst. Technol.* **24** 67–72